Cohesive zone modeling of dynamic failure in homogeneous and functionally graded materials

Zhengyu (Jenny) Zhang, Glaucio H. Paulino *

Department of Civil and Environmental Engineering, University of Illinois at Urbana-Champaign, 2209 Newmark Laboratory, 205 North Mathews Avenue, Urbana, IL 61801, USA

Abstract

This work investigates dynamic failure processes in homogeneous and functionally graded materials (FGMs). The failure criterion is incorporated in the cohesive zone model (CZM) using both a finite cohesive strength and work to fracture in the material description. A novel CZM for FGMs is explored and incorporated into a finite element framework. The material gradation is approximated at the element level using a graded element formulation. Examples are provided to verify the numerical approach, and to investigate the influence of material gradation on crack initiation and propagation in Mode-I as well as in mixed-mode fracture problems. The examples include spontaneous rapid crack growth in homogeneous and FGM strips, dynamic crack propagation in actual monolithic and epoxy/glass FGM beams (three-point bending) under impact loading, and mixed-mode crack propagation in pre-cracked steel and graded plates.
© 2004 Elsevier Ltd. All rights reserved.

Keywords: Finite element method; Graded finite element; Functionally graded material; Graded composites; Intrinsic cohesive zone model; Dynamics; Mixed-mode fracture

---

* Corresponding Author. Tel.: +1 217 333 3817; fax: +1 217 265 8041.
E-mail address: paulino@uiuc.edu (G.H. Paulino).

1. Introduction

Functionally graded materials or FGMs are a new generation of engineered composites characterized by spatially varied microstructures accomplished through non-uniform distribution of the reinforcement phase with different properties, sizes and shapes, as well as by interchanging the roles of reinforcement and matrix (base) materials in a continuous manner. This new concept of engineering the material microstructure and recent advances in material processing science allows one to fully integrate material and structural design considerations (Miyamoto et al., 1999; Paulino et al., 2003).

The initial emphasis for FGMs focused on the synthesis of thermal barrier coatings for aerospace applications, however, subsequent investigations have addressed a wide variety of applications (Suresh and Mortensen, 1998). Many of these applications involve dynamic events such as blast protection for critical structures and armors for ballistic protection. For example, a functionally graded armor composite with a tailored ceramic to metal through-thickness gradient combines the beneficial effects of ceramics (e.g., hardness) and metals (e.g., toughness) in the same material system while suppressing adverse strength reduction that would occur with discrete interfaces (Chin, 1999) – also see (Gooch et al., 1999) for an investigation of functionally graded TiB/Ti armors. Other applications of FGMs include bone and dental implants, piezoelectric and thermoelectric devices, and optical materials with graded refractive indices (Paulino et al., 2003; Suresh and Mortensen, 1998). Parallel to advancements in FGM manufacturing and experimentation, methodologies to evaluate and predict FGM properties and behaviors have been developed. For example, homogenization technique and higher-order theory have been adopted to evaluate effective material properties and responses (Aboudi et al., 1999, 2003; Yin et al., 2004).

Fracture mechanics of FGMs has been an active area of research during recent years (Erdogan, 1995). Eischen investigated mixed-mode cracks in non-homogeneous materials and proposed a path-independent J_2 formulation by incorporating strain energy along the crack surfaces (Eischen, 1987a,b). Dolbow and Gosz (2002) presented an interaction energy integral method for accurate evaluation of mixed-mode stress intensity factors at FGM crack tips. Kim and Paulino (2002a,b,c, 2003, 2004) provided techniques for evaluating mixed-mode stress intensity factors, J-integrals, interaction integrals, T-stress, and crack initiation angles under static and quasi-static conditions for both isotropic and orthotropic materials. To fully exploit their multi-functionality and high performance, further understanding of the dynamic fracture behavior of FGMs is desired, especially when these materials are exposed to hostile environments and subject to impact loading. This area, however, remains fairly unexplored so far.

Among the various numerical schemes addressing static and dynamic fracture problems, cohesive zone models (CZMs) are of growing interest for fracture modeling and are currently widely used in simulations for both homogeneous and non-homogeneous material systems. Various models have been proposed, their advantages, disadvantages and limitations being debated – see (Xu and Needleman,

1995, Geubelle and Baylor, 1998, Zavattieri and Espinosa, 2001; Pandolfi and Ortiz, 2002). CZMs incorporate a cohesive strength and finite work to fracture in the description of material behavior, and allow simulation of near-tip behavior and crack propagation. The concept of "cohesive failure" is illustrated in Fig. 1 for tensile (mode I) case. It is assumed that a *cohesive zone*, along the plane of potential crack propagation, is present in front of the crack tip. Within the extent of the cohesive zone, the material points which were identical when the material was intact, separate to a distance Δ due to influence of high stress state at the crack tip vicinity. The cohesive zone surface sustains a distribution of tractions T which are function of the displacement jump across the surface Δ, and the relationship between the traction T and separation Δ is defined as the constitutive law for the cohesive zone surface. As an example, in the exponential model by Xu and Needleman (1995), the constitutive law indicates that with increasing interfacial separation Δ, the traction T across the cohesive interface first increases smoothly, reaches a maximum value at the critical separation δ, then decreases, and finally vanishes at a characteristic separation value, here denoted as δ_c, where complete decohesion is assumed to occur. The subscript n (normal) is attached to the parameters in Fig. 1 to denote the tensile (Mode I) fracture case. Moreover, in Mode-II or mixed-mode case the tangential traction–separation behavior should be included.

Barenblatt (1959, 1962) proposed the CZM first for perfectly brittle materials that accounted for atomic interaction near a crack tip. Around the same time-frame (Dugdale, 1960) extended the concept to perfectly plastic material by postulating the existence of a process zone at the crack tip region. This model assumes constant cohesive traction (equals to yield strength) along the entire span of the process zone. Afterwards, models considering materials exhibiting progressive softening behavior (thus the traction–separation is a decreasing function) are also developed – see (Bažant and Cedolin, 1991; Bažant and Planas, 1998). Later, the cohesive zone concept was adapted into numerical simulation schemes. For instance, Needleman (1987) considered the inclusion debonding case using a potential-based cohesive traction–separation relationship. Tvergaard (1990) investigated the fiber debonding problem
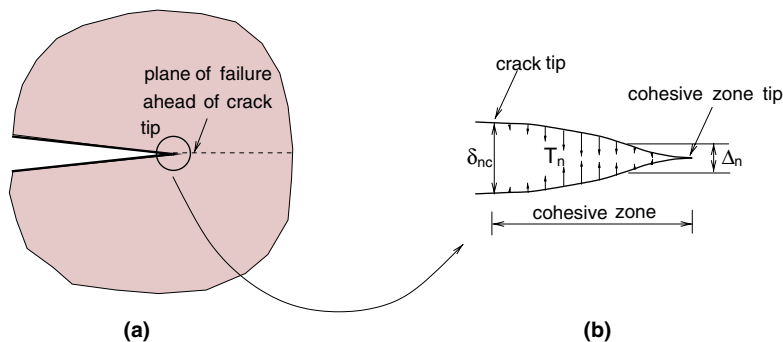

Fig. 1. Schematic representation of: (a) the cohesive zone concept and (b) the cohesive tractions along a cohesive surface at the crack tip vicinity.

considering both normal and tangential separations using a CZM without the potential form. Xu and Needleman (1995) later developed a potential-based model incorporating both normal and tangential traction–separation relationships. This model was widely used later on due to its simplicity and its potential form. It incorporates a hardening part in the traction–separation curve (shown in Fig. 2), which leads to artificial reduction of stiffness. Existing CZMs exhibiting similar behavior include the bilinear model proposed by Geubelle and Baylor (1998) and Zavattieri and Espinosa (2001). Another noteworthy CZM in the literature is the extrinsic model proposed by Camacho and Ortiz (1996), which eliminates the artificial compliance typical of the intrinsic models mentioned above. Ortiz and co-workers developed models for three-dimensional (3-D) fracture growth and fragmentation simulation (Ortiz and Pandolfi, 1999; Ruiz et al., 2001). Depending on implementation, the extrinsic model may lead to time-discontinuous numerical results (Papoulia et al., 2003). The Virtual Internal Bond model (Klein and Gao, 1998; Klein et al., 2000) is occasionally also categorized as a CZM type, which is essentially an elastic continuum model that can simulate material weakening at a high strain region and thus introduce a crack at the weakened region. During recent years, the CZM became an active research field (Brocks and Cornec, 2003). Although the majority of the literature on CZMs addressed fracture analysis in brittle materials, CZMs are also employed to investigate ductile fracture (Cornec et al., 2003; Jin et al., 2003; Li and Chandra, 2003; Tvergaard, 2003). Many models have been proposed that consider increasing physical complexity, e.g., rate-dependent behavior, thermomechanical behavior, damage, fatigue, and viscoelasticity (Knauss and Losi, 1993; Costanzo and Walton, 1997; Lee and Prakash, 1999; Yoon and Allen, 1999; Roe and Siegmund, 2003; Hattiangadi and Siegmund, 2004). There has been discussions and debates over the pros and cons of each model (Falk et al., 2001).

The aforementioned CZM approach has the promise of simulating fracture process where cracking occurs spontaneously. The fracture path and speed become natural outcome of the simulation rather than being specified ad hoc or a priori. In this paper, a novel cohesive zone model developed for FGMs (Jin et al., 2002) is adopted
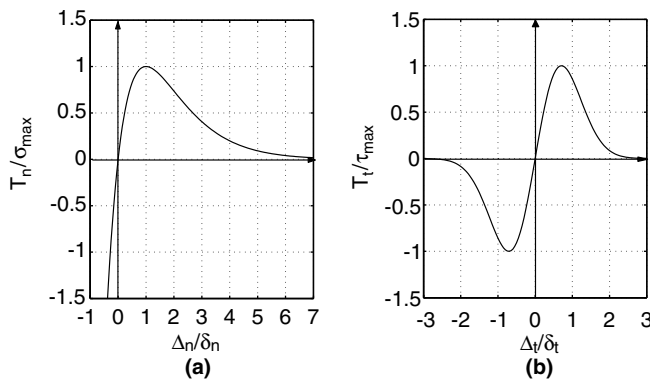

Fig. 2. The *intrinsic* potential-based exponential cohesive model in: (a) pure tension and (b) pure shear.

to simulate dynamic crack growth in FGMs. Section 2 describes the overall dynamic updating scheme and non-homogeneous material approximation methodology used in the investigation, followed by a description of CZMs for FGMs in Section 3. Section 4 presents examples which verify the numerical simulation procedure and illustrate the influence of material variation over dynamic behavior and failure of materials. Thus the behavior is influenced by the length scales introduced by the fracture process and the material gradient – see (Detournay and Garagash, 2003) for a related discussion on scaling. The work presented in this paper focuses on two-dimensional (2-D) fracture.

2. Numerical scheme

The three essential components of cohesive zone modeling of dynamic fracture in FGMs are briefly described here, namely, the dynamic updating scheme, the material gradation and the actual CZM incorporated into finite element scheme. The detailed CZM formulation for FGM will be addressed in Section 3.

2.1. Finite element scheme incorporating cohesive elements

To incorporate a CZM into the numerical scheme for dynamic fracture, the *cohesive element* is developed and implemented as part of the finite element scheme, which follows a cohesive *traction–separation* relationship, e.g., the models discussed in Section 1. In contrast, the conventional finite element, which is now called "*bulk* element", follows conventional *stress–strain* relationships (continuum description).

Fig. 3 illustrates the concept of the two classes of elements (bulk and cohesive). The bulk behavior of the material is accounted for by conventional volumetric elements, whose constitutive relationship is defined, for example, by Hooke's Law. To model fracture initiation and propagation, cohesive elements are positioned along the potential path or region of crack propagation, and attached to the volumetric elements. They are capable of performing decohesion, depending on whether the
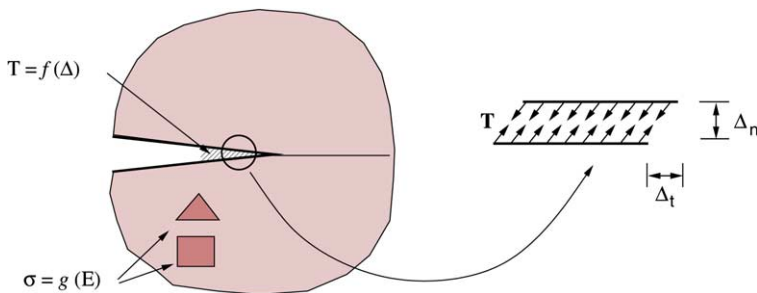

Fig. 3. Schematic representation of *bulk* elements and *cohesive* elements in the finite element formulation. The notation is as follows: T denotes traction, $\Delta = (\Delta_n, \Delta_t)$ denotes separation; σ denotes stress, and E denotes strain.

decohesion force along the cohesive surface has exceeded the cohesive strength. The constitutive law of cohesive elements is inherently embedded in the finite element model, so that the presence of cohesive elements allows spontaneous crack propagation, and thus it is very promising in the investigation of bifurcation and/or impact dynamic loading problem, where multiple crack paths are possible.

2.1.1. Principle of virtual work

The FEM formulation with cohesive elements can be derived from the principle of virtual work, as described below. The principle of virtual work of the dynamic finite element formulation can be expressed as (Xu and Needleman, 1995):

$$\int_{\Omega} (\text{div}\,\boldsymbol{\sigma} - \rho\ddot{\mathbf{u}})\delta\mathbf{u}\,\mathrm{d}\Omega - \int_{\Gamma} (\mathbf{T} - \boldsymbol{\sigma}\mathbf{n})\delta\mathbf{u}\,\mathrm{d}\Gamma = 0, \tag{1}$$

where Ω represents domain area (or volume), Γ denotes boundary line (or surface) with normal vector $\mathbf{n}$, $\mathbf{u}$ is the displacement vector, $\mathbf{T}$ is the traction at the boundary, and $\boldsymbol{\sigma}$ is the Cauchy stress tensor. The superposed dots in $\ddot{\mathbf{u}}$ denote differentiation with respect to time ($\ddot{\mathbf{u}} = \partial^2\mathbf{u}/\partial t^2$), and ρ is the material density. Considering the existence of cohesive surface, applying the divergence theorem and integration by parts to the general expression in (1), one obtains the following expression:

$$\int_{\Omega} (\boldsymbol{\sigma} : \delta\mathbf{E} + \rho\ddot{\mathbf{u}}\cdot\delta\mathbf{u})\,\mathrm{d}\Omega - \int_{\Gamma_{\text{ext}}} \mathbf{T}_{\text{ext}}\cdot\delta\mathbf{u}\,\mathrm{d}\Gamma - \int_{\Gamma_{\text{coh}}} \mathbf{T}_{\text{coh}}\cdot\delta\Delta\mathbf{u}\,\mathrm{d}\Gamma = 0, \tag{2}$$

where Γ_{ext} represents the boundary line on which external traction $\mathbf{T}_{\text{ext}}$ is applied, and $\mathbf{E}$ is the Green strain tensor. The contribution of cohesive traction–separation work is accounted by the last term integrating over the internal cohesive surfaces Γ_{coh} on which the cohesive tractions $\mathbf{T}_{\text{coh}}$ and displacement jumps $\Delta\mathbf{u}$ are present.

The integrals in Eqs. (1) and (2) are carried out in the deformed configuration. When the expression is cast into the undeformed configuration, work conjugates other than $\boldsymbol{\sigma}$ and $\mathbf{E}$ are used instead. With all quantities referred to undeformed configuration, the following expression is obtained instead:

$$\int_{\Omega} (\mathbf{S} : \delta\mathbf{E} + \rho\ddot{\mathbf{u}}\cdot\delta\mathbf{u})\,\mathrm{d}\Omega - \int_{\Gamma_{\text{ext}}} \mathbf{T}_{\text{ext}}\cdot\delta\mathbf{u}\,\mathrm{d}\Gamma - \int_{\Gamma_{\text{coh}}} \mathbf{T}_{\text{coh}}\cdot\delta\Delta\mathbf{u}\,\mathrm{d}\Gamma = 0, \tag{3}$$

where $\mathbf{S}$ denotes the second Piola–Kirchhoff stress tensor, which is related to the Cauchy stress tensor $\boldsymbol{\sigma}$ as follows (e.g., Belytschko et al., 2000)

$$\mathbf{S} = J\mathbf{F}^{-1}\boldsymbol{\sigma}\mathbf{F}^{-\mathrm{T}}, \quad \text{where } J = \det\mathbf{F} \tag{4}$$

and $\mathbf{F}$ denotes the deformation gradient tensor.

2.1.2. Explicit dynamic scheme

In the present work, the explicit central difference time stepping scheme (see, Bathe, 1996; Belytschko et al., 1976) is used, and the updating scheme for nodal displacements, accelerations and velocities from time step (n) to ($n + 1$) is:

$$\mathbf{u}_{n+1} = \mathbf{u}_n + \Delta t\dot{\mathbf{u}}_n + \tfrac{1}{2}\Delta t^2\ddot{\mathbf{u}}_n, \tag{5}$$

$$\ddot{\mathbf{u}}_{n+1} = \mathbf{M}^{-1}(\mathbf{F} - \mathbf{R}_{\text{int}_{(n+1)}} + \mathbf{R}_{\text{coh}_{(n+1)}}), \tag{6}$$

$$\dot{\mathbf{u}}_{n+1} = \dot{\mathbf{u}}_n + \frac{\Delta t}{2}(\ddot{\mathbf{u}}_n + \ddot{\mathbf{u}}_{n+1}), \tag{7}$$

where Δt denotes the time step, $\mathbf{M}$ is the mass matrix, $\mathbf{F}$ is the external force vector, $\mathbf{R}_{\text{int}}$ and $\mathbf{R}_{\text{coh}}$ are the global internal and cohesive force vectors, which are obtained from the contribution of *bulk* and *cohesive* elements, respectively.

2.2. Generalized isoparametric element formulation for FGMs

The formulation described above applies to both homogeneous and FGM problems. To treat the material non-homogeneity inherent in the problem, we can use either homogeneous elements with constant material properties at the element level, which are evaluated at the centroid of each element; or graded elements, which incorporate the material property gradient at the size-scale of the element. Due to the reasons discussed below, the later approach is adopted here.

Two alternative schemes for graded elements have been proposed by Anlas et al. (2000) and Kim and Paulino (2002a). In general, the graded element has been demonstrated to result in smoother and more accurate stresses than the homogeneous elements. In this investigation, the scheme proposed by Kim and Paulino (2002a) is adopted. The same shape functions are used to interpolate the unknown displacements, the geometry, and the material parameters, and hence earned the name *Generalized Isoparametric Element Formulation* or *GIF*. The interpolations for material properties (E, v, ρ) are given by

$$E = \sum_{i=1}^{m} N_i E_i, \quad v = \sum_{i=1}^{m} N_i v_i, \quad \rho = \sum_{i=1}^{m} N_i \rho_i, \tag{8}$$

where N_i are the shape functions.

Both homogeneous and graded elements are implemented in the present code, and graded elements are used to model FGMs. These elements will be particularly beneficial within regions with coarse mesh discretization or with high stress gradients. The bulk elements employed to address the problems presented in this work are T6 elements. The choice of triangular elements rather than quadrilateral elements is because the former elements allow crack growth along more arbitrary directions. The cohesive elements are quadratic line elements, and full integration scheme is used throughout the study.

2.3. Wave speed in FGM and time step control

The stability of conventional explicit finite element schemes is usually governed by the Courant condition (Bathe, 1996), which provides an important upper limit for the size of the time step Δt:

$$\Delta t \leqslant \frac{\ell_{\mathrm{e}}}{C_{\mathrm{d}}}, \tag{9}$$

where ℓ_{e} is the shortest distance between two nodes in the mesh, and the dilatational wave speed C_{d} is expressed in terms of the material elastic constants $E = E(\mathbf{x})$, $v = v(\mathbf{x})$, and density $\rho = \rho(\mathbf{x})$ as

$$C_{\mathrm{d}}(\mathbf{x}) = \sqrt{\frac{E(\mathbf{x})(1 - v(\mathbf{x}))}{(1 + v(\mathbf{x}))(1 - 2v(\mathbf{x}))\rho(\mathbf{x})}} : \quad \text{plane strain}, \tag{10}$$

$$C_{\mathrm{d}}(\mathbf{x}) = \sqrt{\frac{E(\mathbf{x})}{(1 + v(\mathbf{x}))(1 - v(\mathbf{x}))\rho(\mathbf{x})}} : \quad \text{plane stress}. \tag{11}$$

The presence of cohesive elements requires the time step to be further decreased in order to assure computational stability, due to discontinuous wave propagation across the cohesive surfaces. The reduction of time step depends on the element size, cohesive strength, and material stiffness (Baylor, 1998; Zhang, 2003). Because material properties for non-homogeneous materials (e.g., FGMs) vary in space, C_{d} is no longer a constant. To simplify the implementation, the maximum wave speed is calculated depending on the profile of the material property, and a uniform maximum time step is applied to the whole structure.

3. Cohesive zone model for FGMs

A volume-fraction based phenomenological cohesive zone model for FGM that introduces two material specific parameters to account for the interaction between different material phases was presented by Jin et al. (2002). This effective model is briefly described in Section 3.1. A related model (Zhang, 2003) is proposed in Section 3.2, which is based on actual quantities (rather than effective ones). A bilinear model is presented in Section 3.3, which alleviates the artificial compliance problem by allowing adjustment of its initial stiffness. Besides, when certain assumptions of these models differ from the experimental observations, another approach is taken, which is described in Section 3.4.

3.1. Cohesive model using effective traction–separation

The notation below follows the paper by Jin et al. (2002), except for the substitution of the subscripts "met" and "cer", which originally denoted metal and ceramic phases, to "1" and "2", so that the notation is more general. The model by Jin et al. (2002) uses effective displacement jump Δ_{eff} and effective cohesive traction T_{eff} when dealing with mixed mode fracture, which are defined as

$$\Delta_{\mathrm{eff}} = \sqrt{\Delta_{\mathrm{n}}^2 + \eta^2 \Delta_{\mathrm{t}}^2}, \tag{12}$$

$$T_{\text{eff}} = \sqrt{T_{\text{n}}^2 + \eta^{-2} T_{\text{t}}^2}, \tag{13}$$

where Δ_{n} and Δ_{t} denote the normal and tangential displacement jumps across the cohesive surface, and T_{n} and T_{t} denote the corresponding normal and shear tractions across the cohesive surface. The parameter η assigns different weights to the opening and sliding displacements and it is the ratio of tangential cohesive strength $T_{\text{t}}^{\max}$ to normal cohesive strength $T_{\text{n}}^{\max}$, i.e., $\eta = T_{\text{t}}^{\max} / T_{\text{n}}^{\max}$.

With these two effective quantities introduced, the energy potential in 2-D case takes the form

$$\phi_{\text{fgm}}(\mathbf{x}, \Delta_{\text{eff}}) = \frac{V_1(\mathbf{x})}{V_1(\mathbf{x}) + \beta_1[1 - V_1(\mathbf{x})]} e T_1^{\max} \delta_1 \left[1 - \left(1 + \frac{\Delta_{\text{eff}}}{\delta_1} \right) \exp \left(-\frac{\Delta_{\text{eff}}}{\delta_1} \right) \right]$$
$$+ \frac{1 - V_1(\mathbf{x})}{1 - V_1(\mathbf{x}) + \beta_2 V_1(\mathbf{x})} e T_2^{\max} \delta_2 \left[1 - \left(1 + \frac{\Delta_{\text{eff}}}{\delta_2} \right) \exp \left(-\frac{\Delta_{\text{eff}}}{\delta_2} \right) \right], \tag{14}$$

where $T_i^{\max}$ and δ_i denote the maximum cohesive traction and the corresponding displacement jump value Δ at $T_1 = T_1^{\max}$ for material phase i, $i = 1,2$. The parameter $V_1(\mathbf{x})$ denotes volume fraction of the material phase 1, while β_1 and β_2 are two cohesive gradation parameters that describe the transition of failure mechanisms from pure material phase 1 to pure material phase 2. With the above formulation, the cohesive traction reduces to that of the material 1 when $V_1 = 1$ and to that of the material 2 when $V_1 = 0$, as expected. The two additional parameters, β_1 and β_2, which are material-dependent, should be calibrated by experiments. For instance, by conducting fracture test of FGMs using standard specimen geometries, e.g., compact tension (CT) test, fracture behavior of the material can be measured (e.g., load versus crack extension length relationship), and compared with numerical simulations using different β_1 and β_2 values. For instance, the TiB/Ti FGM CT specimens with parameters $\beta_2 = 1$ and $\beta_1 = 1, 3, 5$, respectively, were simulated, and load-crack extension responses were reported in Jin et al. (2002). Their results indicate that the fracture resistance reduces with increasing β_1. Hence, once the same test is performed on actual TiB/Ti fracture specimens, the values of parameters β_1 and β_2 can be determined by matching the experimental results and the computational ones. The normal and tangential cohesive traction thus follows:

$$T_{\text{n}} = \frac{\partial \phi_{\text{fgm}}}{\partial \Delta_{\text{n}}} = \frac{\partial \phi_{\text{fgm}}}{\partial \Delta_{\text{eff}}} \frac{\partial \Delta_{\text{eff}}}{\partial \Delta_{\text{n}}} = \left(\frac{T_{\text{eff}}}{\Delta_{\text{eff}}} \right) \Delta_{\text{n}}, \tag{15}$$

$$T_{\text{t}} = \frac{\partial \phi_{\text{fgm}}}{\partial \Delta_{\text{t}}} = \frac{\partial \phi_{\text{fgm}}}{\partial \Delta_{\text{eff}}} \frac{\partial \Delta_{\text{eff}}}{\partial \Delta_{\text{t}}} = \eta^2 \left(\frac{T_{\text{eff}}}{\Delta_{\text{eff}}} \right) \Delta_{\text{t}}, \tag{16}$$

where

$$T_{\text{eff}} = \frac{\partial \phi_{\text{fgm}}}{\partial \Delta_{\text{eff}}}$$

$$= \frac{V_1(\mathbf{x})}{V_1(\mathbf{x}) + \beta_1[1 - V_1(\mathbf{x})]} e T_1^{\max} \left(\frac{\Delta_{\text{eff}}}{\delta_1}\right) \exp\left(-\frac{\Delta_{\text{eff}}}{\delta_1}\right)$$

$$+ \frac{1 - V_1(\mathbf{x})}{1 - V_1(\mathbf{x}) + \beta_2 V_1(\mathbf{x})} e T_2^{\max} \left(\frac{\Delta_{\text{eff}}}{\delta_2}\right) \exp\left(-\frac{\Delta_{\text{eff}}}{\delta_2}\right)$$

if $\Delta_{\text{eff}} = \Delta_{\text{eff}}^{\max}$ and $\dot{\Delta}_{\text{eff}} \geqslant 0$: loading, (17)

in which $\Delta_{\text{eff}}^{\max}$ is the maximum value of Δ_{eff} attained in loading history, and

$$T_{\text{eff}}(x) = \left(\frac{T_{\text{eff}}^*}{\Delta_{\text{eff}}^{\max}}\right) \Delta_{\text{eff}} \quad \text{if } \Delta_{\text{eff}} < \Delta_{\text{eff}}^{\max} \text{ or } \dot{\Delta}_{\text{eff}} < 0: \quad \text{unloading.} \quad (18)$$

Notice that T_{eff}^* is the value of T_{eff} at $\Delta_{\text{eff}} = \Delta_{\text{eff}}^{\max}$ computed from Eq. (17). The loading–unloading condition is introduced to retain irreversibility of fracture path, as illustrated in Fig. 4(a).

The cohesive force–displacement relationships of material phases 1 and 2 are illustrated in Fig. 4, where it is obvious that the cohesive energy (the area under cohesive curve) for material phase 2 (e.g., ceramic phase), is only a small portion of that for material phase 1 (e.g., metal phase).

3.2. Cohesive model using actual traction–separation

The model described above (Jin et al., 2002) was used to investigate quasi-static crack growth in Ti/TiB FGMs. Its merits include simplicity and a straightforward
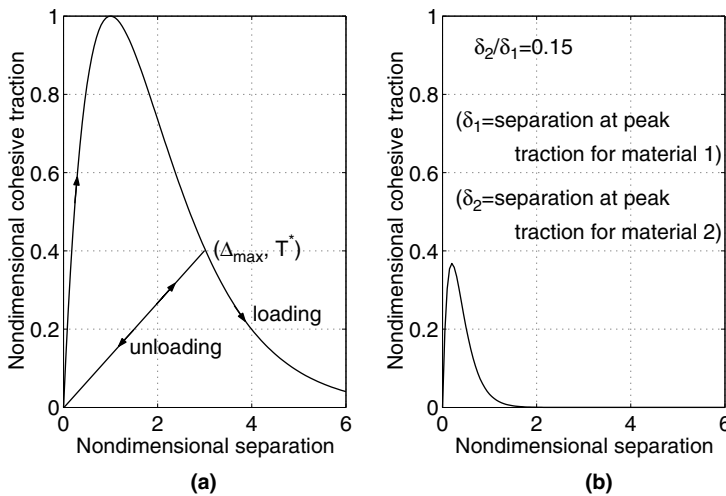

Fig. 4. Normalized cohesive traction versus normalized separation displacement, in which the strength ratio of the two material phases, $T_2^{\max}/T_1^{\max}$, is taken as 0.35; (a) $T_1/T_1^{\max}$ versus Δ/δ_1 for material phase 1; (b) $T_2/T_1^{\max}$ versus Δ/δ_1 for material phase 2.

formulation in 3-D. However, whether its "effective" feature works for mixed-mode problems remains an issue, as all the problems under investigation in Jin et al. (2002) were Mode-I problems, and cohesive elements were prescribed along the fracture plane that is subjected to pure Mode-I loading. Care needs to be taken when using this model to deal with mixed-mode problems. When Mode-II fracture is involved (even for homogeneous material), the local fracture behavior becomes involved and depends on the material microstructure, since the grain size, shape, surface roughness, etc. affect the friction behavior when sliding occurs. Moreover, the above effective model by Jin et al. (2002) does not differentiate the material toughness in Mode-I and Mode-II. Although the parameter η indicates different cohesive strengths of the two modes, the critical displacement jumps for the two modes are also in proportional relationship, resulting in the same Mode-I and Mode-II fracture energy. Therefore, a new FGM cohesive zone model is proposed which uses the actual quantities to describe the traction–separation relationship along normal and tangential directions, respectively. To this end, the Xu and Needleman (1995) model is extended to the FGM case, and material parameters similar to those by Jin et al. (2002) are introduced in the FGM model to account for material interaction.

Assume that the energy potential of each individual material phase takes the exponential form (Xu and Needleman, 1995):

$$\phi_1(\mathbf{\Delta}) = \phi_{n1} + \phi_{n1} \exp\left(-\frac{\Delta_n}{\delta_{n1}}\right)$$
$$\times \left\{ \left[1 - r_1 + \frac{\Delta_n}{\delta_{n1}}\right] \frac{(1-q_1)}{(r_1-1)} - \left[q_1 + \frac{(r_1-q_1)}{(r_1-1)} \frac{\Delta_n}{\delta_{n1}}\right] \exp\left(-\frac{\Delta_t^2}{\delta_{t1}^2}\right) \right\}, \quad (19)$$

$$\phi_2(\mathbf{\Delta}) = \phi_{n2} + \phi_{n2} \exp\left(-\frac{\Delta_n}{\delta_{n2}}\right)$$
$$\times \left\{ \left[1 - r_2 + \frac{\Delta_n}{\delta_{n2}}\right] \frac{(1-q_2)}{(r_2-1)} - \left[q_2 + \frac{(r_2-q_2)}{(r_2-1)} \frac{\Delta_n}{\delta_{n2}}\right] \exp\left(-\frac{\Delta_t^2}{\delta_{t2}^2}\right) \right\} \quad (20)$$

in which superscripts 1 and 2 denote the two individual material phases (e.g., metal and ceramic, respectively), and parameters $\mathbf{\Delta} = [\Delta_n, \Delta_t]$ denote the displacement jump across the cohesive surface in normal and tangential directions. Other parameters in the expressions that, respectively, refer to material phases 1 and 2 are explained hereby without subscript (1 or 2) notation: parameters ϕ_n and ϕ_t are the energies required for pure normal and tangential separation, respectively; δ_n and δ_t are the critical opening displacement for normal and tangential separation, which are related to the cohesive normal strength T_n^{max} and tangential strength T_t^{max} as

$$\phi_n = eT_n^{max}\delta_n, \quad \phi_t = \sqrt{e/2}T_t^{max}\delta_t, \quad (21)$$

$q = \phi_t/\phi_n$, and r is defined as the value of Δ_n/δ_n after complete shear separation with $T_n = 0$. The cohesive traction force vectors associated with material phases 1 and 2 in the 2-D case comprise traction in normal and tangential directions:

$$\mathbf{T}_1 = [T_{n1}, T_{t1}], \quad \mathbf{T}_2 = [T_{n2}, T_{t2}],$$

and can be derived directly from the energy potentials as follows:

$$\mathbf{T}_1 = -\frac{\partial \phi_1}{\partial \mathbf{\Delta}}, \quad \mathbf{T}_2 = -\frac{\partial \phi_2}{\partial \mathbf{\Delta}}. \tag{22}$$

The resulting normal and shear traction components are obtained as (subscripts omitted)

$$T_n = -\frac{\phi_n}{\varDelta_n}$$
$$\times \exp\left(-\frac{\varDelta_n}{\delta_n}\right) \left\{ \frac{\varDelta_n}{\delta_n} \exp\left(-\frac{\varDelta_t^2}{\delta_t^2}\right) + \frac{(1-q)}{(r-1)} \left[1 - \exp\left(-\frac{\varDelta_t^2}{\delta_t^2}\right) \right] \left[r - \frac{\varDelta_n}{\delta_n} \right] \right\}, \tag{23}$$

$$T_t = -\frac{\phi_n}{\varDelta_n} \left(2\frac{\delta_n}{\delta_t} \right) \frac{\varDelta_t}{\delta_t} \left\{ q + \frac{(r-q)}{(r-1)} \frac{\varDelta_n}{\delta_n} \right\} \exp\left(-\frac{\varDelta_n}{\delta_n}\right) \exp\left(-\frac{\varDelta_t^2}{\delta_t^2}\right) \tag{24}$$

for each material phase. Let

$$\mathbf{T}_{FGM} = \left[T_n^{FGM}, T_t^{FGM} \right]$$

denote the traction force vector across the cohesive surfaces of a two-phase FGM, which comprises normal and tangential traction force component. The cohesive traction $\mathbf{T}_{FGM}$ is approximated by the following volume fraction-based formula

$$\mathbf{T}_{FGM}(\mathbf{x}) = \frac{V_1(\mathbf{x})}{V_1(\mathbf{x}) + \beta_1[1 - V_1(\mathbf{x})]} \mathbf{T}_1 + \frac{1 - V_1(\mathbf{x})}{1 - V_1(\mathbf{x}) + \beta_2 V_1(\mathbf{x})} \mathbf{T}_2, \tag{25}$$

where the material parameters β_1 and β_2 account for the reduction of fracture toughness due to interaction of material phases, and should be calibrated with experimental data.

When both materials have the same properties and parameters $\beta_1 = \beta_2 = 1$, the above formulation reduces to that of Xu and Needleman (1995) model for homogeneous materials. This model avoids effective quantities like effective separation $\varDelta_{eff}$, which is dubious for FGM problems (due to the complicated microstructure-induced fracture mechanisms). The main drawback is that two additional material parameters, used for the tangential cohesive strength T_t^{max} and associated energy ϕ_t, are needed in comparison to the earlier effective model by Jin et al. (2002).

3.3. Bilinear cohesive model

As discussed in the literature (e.g., Baylor, 1998, Klein et al., 2000, Zhang, 2003), insertion of cohesive elements introduces fictitious compliance to the structure. This effect is inherent to the "intrinsic" CZM approach. However, if carefully treated, this unwelcome effect can be restricted to certain limits within which extent the numerical analysis can still reliably simulate the problem. The magnitude of artificial

compliance introduced is primarily related to the initial slope of the traction–separation law. A stiffer slope represents more rigid initial bonds between bulk elements, resulting in less fictitious compliance. To minimize mesh size dependence, the compliance introduced to the system should ideally be the same for various mesh discretizations. This requirement is difficult to satisfy for the Xu and Needleman (1995) model, for which the traction–separation law has a defined shape, and thus defined initial slope.

A bilinear cohesive model is thus adopted in favor of its adjustable slope attribute. Zavattieri and Espinosa (2001) presented a bilinear cohesive zone model, for which the material fails when the parameter λ (which is a function of the normal and tangential separations) reaches the unity. Here, we specialize the expression for λ as follows:

$$\lambda = \sqrt{\left(\frac{\Delta_n}{\delta_n}\right)^2 + \left(\frac{\Delta_t}{\delta_t}\right)^2}. \tag{26}$$

The parameters Δ_n, Δ_t are the current normal and tangential cohesive interface separations, while δ_n, δ_t are the critical separation values at which the interface is considered to have failed in the two modes, respectively. Similarly to the model by Geubelle and Baylor (1998), the choice of a "critical separation" λ_{cr} allows the users to specify the initial slope of the cohesive law. Apparently, the value of λ_{cr} ought to be close to zero to ensure initially stiff cohesive bonds. The cohesive law is stated as

$$T_n = T_n^{max} \frac{\Delta_n}{\delta_n} \frac{1 - \lambda^*}{\lambda^*(1 - \lambda_{cr})}, \tag{27}$$

$$T_t = T_t^{max} \frac{\Delta_t}{\delta_t} \frac{1 - \lambda^*}{\lambda^*(1 - \lambda_{cr})}, \tag{28}$$

where λ^* is defined as

$$\lambda^* = \begin{cases} \lambda_{cr} & \text{if } \lambda \leqslant \lambda_{cr}, \\ \lambda & \text{if } \lambda > \lambda_{cr}. \end{cases}$$

The traction–separation relationships for pure Mode I and pure Mode II cases are plotted in Fig. 5. In Fig. 5(a), the traction–separation relationship in the compression region has the same slope as in the tension region. To maintain irreversibility of interface weakening, the parameter λ is set to retain its maximum value throughout the loading history.

$$\lambda = \max(\lambda_{current}, \lambda_{previous}).$$

In order to simulate crack propagation in FGM, we extended the bilinear model of Fig. 5 to incorporate material gradation using material dependent parameters as described in Section 3.2. The cohesive traction vector for FGM ($\mathbf{T}_{FGM}$) is approximated by the volume fraction-based formula, Eq. (25), and the traction forces associated with each material phase ($\mathbf{T}_1$ and $\mathbf{T}_2$) are determined from Eqs. (27)
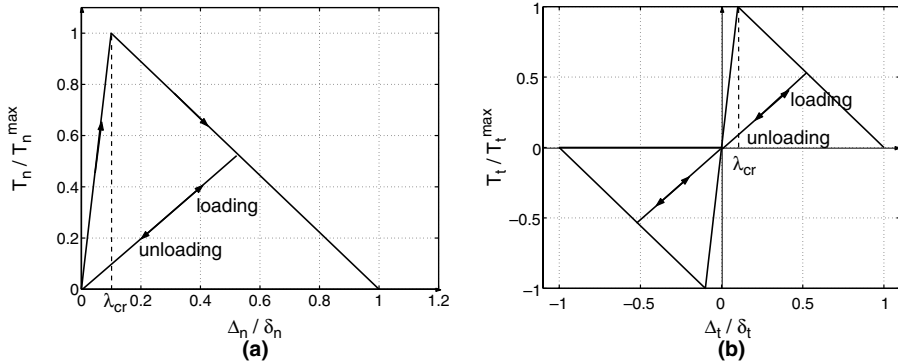
Fig. 5. Bilinear cohesive model: (a) pure normal traction–separation and (b) pure tangential traction–separation.

and (28), while the separation parameter λ (Eq. (26)) is evaluated for each material phase. The following expressions thus follow:

$$
T_n^{FGM}(\mathbf{x}) = \frac{V_1(\mathbf{x})}{V_1(\mathbf{x}) + \beta_1[1 - V_1(\mathbf{x})]} T_{n1}^{max} \frac{\Delta_n}{\delta_{n1}} \frac{1 - \lambda_1^*}{\lambda_1^*(1 - \lambda_{cr1})}
$$
$$
+ \frac{1 - V_1(\mathbf{x})}{1 - V_1(\mathbf{x}) + \beta_2 V_1(\mathbf{x})} T_{n2}^{max} \frac{\Delta_n}{\delta_{n2}} \frac{1 - \lambda_2^*}{\lambda_2^*(1 - \lambda_{cr2})}, \tag{29}
$$

$$
T_t^{FGM}(\mathbf{x}) = \frac{V_1(\mathbf{x})}{V_1(\mathbf{x}) + \beta_1[1 - V_1(\mathbf{x})]} T_{t1}^{max} \frac{\Delta_t}{\delta_{t1}} \frac{1 - \lambda_1^*}{\lambda_1^*(1 - \lambda_{cr1})}
$$
$$
+ \frac{1 - V_1(\mathbf{x})}{1 - V_1(\mathbf{x}) + \beta_2 V_1(\mathbf{x})} T_{t2}^{max} \frac{\Delta_t}{\delta_{t2}} \frac{1 - \lambda_2^*}{\lambda_2^*(1 - \lambda_{cr2})}, \tag{30}
$$

where the subscripts 1 and 2 denote the two material phases, and the other material parameters $V_1(\mathbf{x})$, β_1 and β_2 follow the same definitions as in Section 3.2.

3.4. Cohesive model employing experimental fracture toughness data

The above two cohesive zone models for FGMs introduce additional material parameters to account for the reduction of cohesive strength due to interaction between constituent components. Such phenomenological models can be employed when experimental fracture toughness data are available for *individual* material constituents (monolithic materials), and also for the FGMs. However, there are instances in which the FGM data should be employed explicitly in the simulation. This happens, for example, for the real epoxy/glass FGM system tested by Rousseau and Tippur (2001a). The above three models, with their specific prescriptions of the introduced material parameters, assume monotonically increasing critical energy release rate as the volume fraction of the tougher phase increases. However, the

fracture test (Rousseau and Tippur, 2001a) reveals a different trend. This observation motivates the fourth CZM approach for FGMs in which the fracture toughness becomes a direct input into the numerical simulation, instead of being computed from individual components by either mixture or micromechanics relations. Section 4.2 provides further detail of this issue.

4. Numerical examples

Three examples are provided to illustrate the application of the cohesive models introduced above to both homogeneous and FGM systems. For the first two problems, small deformation is employed because the fracture process is relatively simple: it is Mode-I controlled, and the crack path is restrained along a pre-defined line; moreover, the objectives of the simulations are still achieved using such assumption. For the third example, which simulates crack propagation under mixed-mode conditions, the cohesive elements are inserted in a large region, and finite deformation is employed (Zhang, 2003) to simulate crack propagation involving finite rotations at the crack tip region. The examples are briefly discussed below.

- *Spontaneous rapid crack growth in homogeneous and FGM strips.* This example investigates the influence of mesh refinement, orientation on the simulation results, as well as energy balance, which provides valuable insight into the energy exchange in the fracture process. Further, crack nucleation is simulated for the strip without an initial crack using the CZM approach. The cohesive model used in this problem is the effective model described in Section 3.1. Because this example involves Mode I fracture only, either the model of Section 3.1 or Section 3.2 provide the same results.
- *Dynamic fracture propagation of monolithic and FGM beams under impact loading.* This example provides an opportunity to employ *real* FGM material parameters and compares results of the present numerical analysis with those of the experiments by Rousseau and Tippur (2001a). The cohesive model used in this problem is the one described in Section 3.4 using experimental fracture toughness data. Small deformation assumption is used in the finite element formulation.
- *Mixed-mode crack growth in steel and FGM plates.* The dynamic crack propagation in homogeneous materials is based on the experiments by Kalthoff and Winkler (1987). The cohesive model used in this problem is the bilinear model of Section 3.3. Finite deformation assumption is used in the finite element formulation.

4.1. Spontaneous rapid crack growth in homogeneous and FGM strips

A strip with a semi-infinite crack subjected to uniform normal displacement at clamped upper and lower edges has been employed to illustrate path-independent

J calculation in static case (Rice, 1968) and dynamic case (Freund, 1998). A similar problem setting which uses finite strip and initial crack was employed by Baylor (1998) to investigate the bilinear cohesive model. In this section, the same problem is investigated for homogeneous as well as graded material systems. Features of the rapid propagation of a straight crack along a predefined path inside the finite strip subjected to initial stretch is studied. First, the mesh convergence of the numerical method is investigated. Results of the crack tip velocity reveal a criterion for mesh size versus crack tip process zone size that depends upon material properties. Next, energy balance is investigated in detail, which also provides verification information for the numerical implementation. Afterwards, graded material property is adopted to investigate the influence of material variation. Moreover, to further explore the capability of simulating spontaneous crack nucleation, the elastic strip *with* initial strain problem is extended to the FGM case *without* initial crack prescribed. By manipulating material properties of the FGM strip, the crack can nucleate at the high stress region and propagate thereafter.

4.1.1. Problem description

The geometry and boundary conditions for the strip problem are illustrated in Fig. 6. The strip is initially stretched uniformly by imposing an initial displacement field

$$u(x, y; t = 0) = 0, \quad v(x, y; t = 0) = \epsilon_0 y, \tag{31}$$

which results in a uniform strain field at the initial time. The upper and lower surfaces are held fixed and a small crack length *a* is introduced at the left edge at time *t* = 0. For the homogeneous strip case, the material is taken as polymethylmethacrylate (PMMA) (Xu and Needleman, 1995), and its properties are given in Table 1. For the FGM problem, the detailed material properties are described for each case in later sections.

4.1.2. Mesh convergence

The domain is discretized uniformly by T6 elements of various element sizes as shown in Fig. 7 and Table 2. Cohesive elements are inserted along the mid-plane
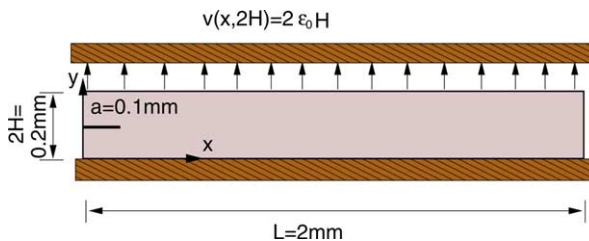

Fig. 6. Domain and boundary conditions of the strip for dynamic fracture simulation.

Table 1
Material properties for PMMA Xu and Needleman (1995) strip subjected to initial stretch

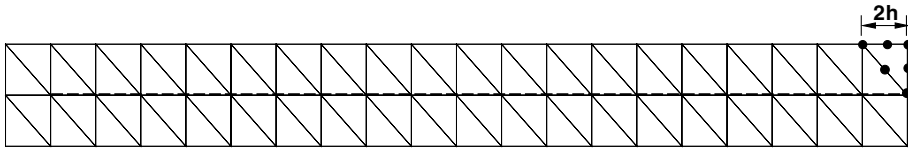| E (GPa)	v	ρ (kg/m^3)	G_{Ic} (N/m)	T_{max} (MPa)	δ (μm)	C_R (m/s)
3.24	0.35	1190	352.3	324	0.4	939

Fig. 7. Mesh discretization with T6 elements for elastic strip subjected to initial stretch. Cohesive elements are inserted at half-height, along the horizontal direction (dashed line), and h is defined as distance between nearest nodes of the cohesive element. This figure shows a coarse mesh with $h = 50$ μm.

Table 2
Mesh discretization associated with Fig. 7

Mesh	h (μm)	# Nodes	# Bulk elements	# Cohesive elements
(a)	50	246	80	19
(b)	25	810	320	38
(c)	16.7	1694	720	57
(d)	12.5	2898	1280	76
(e)	8.33	6566	2882	114
(f)	6.25	10,914	5120	152
(g)	5.56	13,718	6480	171

$y = H$ in order to constrain the crack path along its original plane and prevent crack branching.

Driven by the strain energy stored in the pre-stretched strip, the crack quickly propagates along the predefined path. In actual applications, unless the crack path is constrained, the crack tip speed can hardly reach 50% of Rayleigh wave speed due to energy dissipation mechanisms, for example, from void growth and micro cracks formation at the immediate crack tip vicinity. However, the theoretical crack tip speed is the Rayleigh speed, and for the problem under consideration, as the initial stretch increases, the strain energy stored in the system also increases, and thus the fracture speed approaches the Rayleigh speed C_R of PMMA, which is 939 m/s.

It is essential to investigate the convergence of the numerical scheme in terms of the relation between the characteristic cohesive length scale δ and mesh size h. Here h is defined as the minimum nodal distance of cohesive elements (see Fig. 7). Since quadratic elements are used, one element length equals $2h$. A static analysis estimate of the cohesive zone size for a constant traction–separation relation (Rice, 1968) is

$$\ell_k = \frac{\pi}{8} \frac{E}{1 - v^2} \frac{G_{\text{Ic}}}{T_{\text{ave}}^2}, \tag{32}$$

where for the exponential cohesive law, $T_{\text{ave}} = 0.453 T_{\text{max}}$. For PMMA (Table 1), the estimated cohesive zone size is $\ell_k = 23.6$ μm.

The influence of mesh size on the evolution of the crack tip position is shown in Fig. 8 for an initial stretching parameters $\epsilon_0 = 0.035$. The crack tip is defined as the right-most point along the fracture plane for which $\Delta \approx 6\delta$, where Δ denotes the interface displacement jump.

Evidently, mesh size plays an important role in the spontaneous propagation of fast cracks. To drive the crack to propagate through the whole length of strip, the minimum initial stretch can be estimated as $\epsilon_0 = 0.031$. The detailed derivation will be given in the energy balance discussion. Therefore, for $\epsilon_0 = 0.035$ case in Fig. 8, the initial strain energy stored in the elastic strip is high enough to drive the crack to propagate through the whole strip. However, when the mesh is too coarse ($h = 50$ μm), the crack does not propagate at all. As the mesh is progressively refined (see Table 2), the solution converges as shown in Fig. 8. The curve for velocity $C_{\text{crack}} = C_R$ is an ideal case in which the crack starts to propagate at $t = 0$ through the crack path at Rayleigh wave speed.

For $\epsilon_0 = 0.035$ case, the following three meshes produce very close results in terms of simulation time for the crack to propagate through the strip: $h = 5.56$ μm, $h = 6.25$ μm and $h = 8.33$ μm, and the following two meshes also give good results: $h = 12.5$ μm, $h = 16.7$ μm, which differ from the result given by the mesh with $h = 5.56$ μm only by 5% and 7%, respectively. The results for various mesh refinement and initial
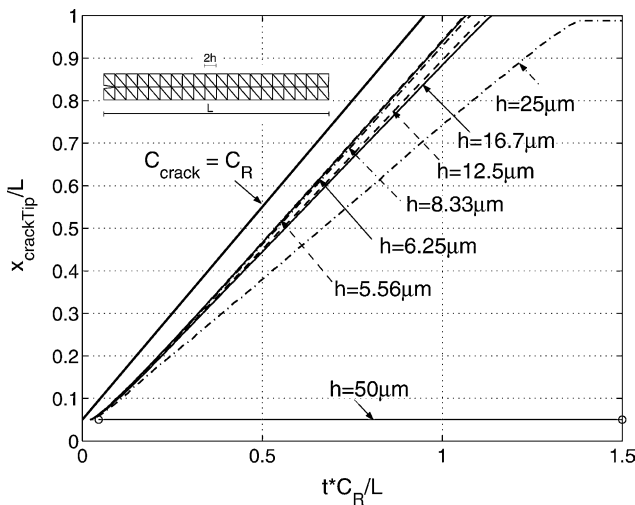

Fig. 8. Normalized crack tip location versus normalized time considering initial stretch $\epsilon_0 = 0.035$ and various levels of mesh refinement. The notation C_R denotes the Rayleigh wave speed ($C_R = 939$ m/s for PMMA).

stretches suggest that the characteristic element size should be chosen two or three times smaller than the cohesive zone size to ensure convergence. For example, for this strip problem, when $h \leqslant 8.33$ μm, which is around one third of the estimated cohesive zone size, the results are acceptable. This is consistent with suggestions made by other researchers (Geubelle and Baylor, 1998; Klein et al., 2000). Moreover, this requirement can be relaxed for some particular cases. For instance, for this strip problem, at sufficiently high initial stretch, a larger cohesive element size can produce converged result, but it is difficult to generalize this observation to other problems.

A similar test is performed to model crack arrest under dynamic conditions, as depicted in Fig. 9, which shows the effect of initial stretching of the elastic strip on the crack propagation. When a sufficient amount of energy is stored initially in the system and adequately refined mesh is used in the simulation, the crack speed approaches the Rayleigh wave speed C_R. For instance, for $\epsilon_0 = 0.5$, the crack tip speed, i.e., the slope of the curve, is almost parallel to that of the ideal case where crack tip speed equals Rayleigh wave speed ($C_{crack} = C_R$ curve). However, for initial stretch $\epsilon_0 < 0.031$, the crack arrests.

4.1.3. Mesh orientation

The results presented in Figs. 8 and 9 are obtained for the meshes shown in Fig. 7, which has a certain mesh orientation bias, i.e., the diagonal lines that bisect the quads into T6 elements are all aligned in the $-45°$ direction, with respect to the Cartesian coordinate x. To address whether a specific mesh orientation influences the computational results in the current problem, two additional mesh orientations are employed to simulate the same problem. They are plotted in Fig. 10, for diagonal
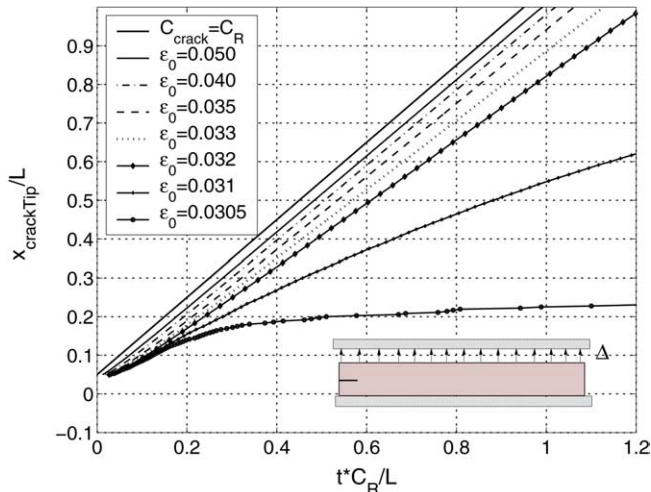

Fig. 9. Normalized crack tip location versus normalized time for various initial stretching parameter ϵ_0. The notation C_R denotes the Rayleigh wave speed ($C_R = 939$ m/s for PMMA).

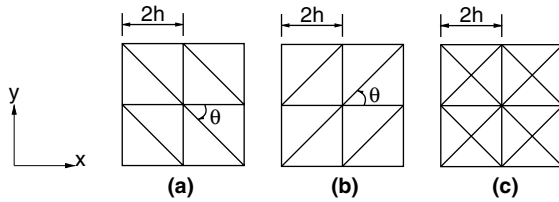Fig. 10. Three mesh orientations: (a) $\theta = -45°$, (b) $\theta = 45°$ and (c) Union-Jack mesh.

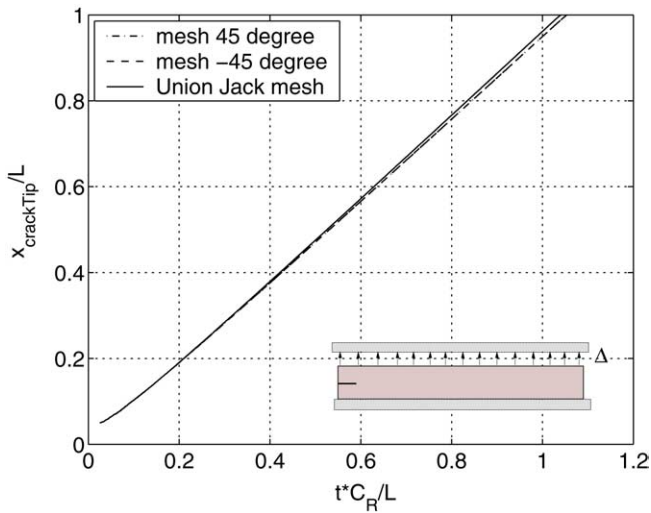Fig. 11. Normalized crack tip location versus time for three different mesh orientations according to Fig. 10; initial stretch $\epsilon_0 = 0.035$, and characteristic cohesive element size $h = 5.56$ μm.

lines in 45° direction with respect to the Cartesian coordinate x (Fig. 10(b)), and "Union-Jack" mesh configuration (Fig. 10(c)).

The numerical simulations are performed using a mesh with $h = 5.56$ μm. Since the cohesive elements are inserted along a predefined straight line and are of the same characteristic size in all three meshes, the results are expected to be similar. This is verified by the results in Fig. 11, which compare the crack tip location of the three meshes, for the initial stretch $\epsilon_0 = 0.035$. Apparently, the results of the two 'biased' meshes, in the sense that the elements are not symmetric with respect to the Cartesian coordinate x, coincide with each other within plotting accuracy, while the "Union-Jack" mesh result is slightly different, especially at longer time.

4.1.4. Energy balance and verification of results

The elastic strip problem presents an appropriate example to examine conversion among energies during dynamic fracture. There are two analytical solutions available that allow verification of the computational results. First, the initial boundary

condition is such that an analytical evaluation of the initial strain energy is easily obtained. Second, the cohesive elements are prescribed along a defined path, hence the total fracture energy required for the crack to propagate through the entire strip can be readily computed. Moreover, the dissipated fracture energy presents a large portion of the total initial energy, and thus the conversion between the stored strain energy and dissipated fracture energy is evident.

4.1.4.1. Energy balance expression. There are a total of six energy components of interest, i.e.,

- External work ($\mathscr{E}_{ext}$): work done by external loading.
- Kinetic energy (K): energy of motion.
- Strain energy due to elastic deformation of the bulk elements (U_{bulk}): elastic energy stored in the bulk material.
- Deformation energy due to elastic deformation of the cohesive elements (U_{coh}): elastic energy stored in the cohesive surfaces.
- Total cohesive energy ($\mathscr{E}_{coh}$): sum of elastic cohesive energy (recoverable) and dissipated fracture energy (irrecoverable).
- Fracture energy ($\mathscr{E}_{frac}$): energy dissipated by the generation of new surfaces to form advancing crack(s).

For the current problem under discussion, the external work is kept constant, with value equal to the initial strain energy due to deformation. At any time instant, the total energy in the system is conserved, i.e.,

$$\mathscr{E}_{tot} = U + K + \mathscr{E}_{frac} = \text{const.}, \tag{33}$$

where

$$U = U_{bulk} + U_{coh} \tag{34}$$

represents the total recoverable elastic energy of the system.

4.1.4.2. Initial strain energy. For the above described initial condition, i.e., uniform stretch along the Cartesian *y*-direction at *t* = 0, the strain energy stored in the strip can be obtained analytically as:

$$U_{bulk} = w \times A = \tfrac{1}{2}\sigma_{ij}\epsilon_{ij} \times A = \tfrac{1}{2}\sigma_{yy}\epsilon_{yy} \times A = \frac{1}{2}\frac{E}{1-v^2}\epsilon_{yy}^2 \times A, \tag{35}$$

where w denotes strain energy density and A is the strip area. Since the initial stretch is only along the *y*-direction, all stress and strain components vanish except σ_{yy} and ϵ_{yy}. When the initial stretch $\epsilon_0 = 0.032$, the strain energy calculated from the analytical expression (35) and the finite element method (FEM) are

$$U_{bulk} = 0.756184615 \text{ N m}, \quad U_{bulk}^{FEM} = 0.756184642 \text{ N m},$$
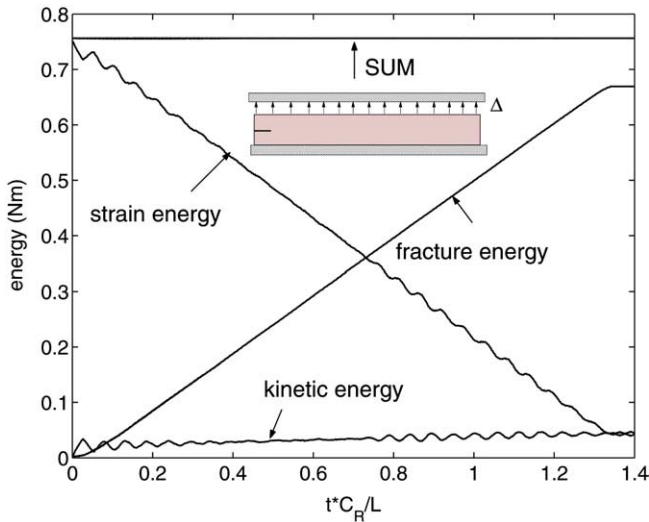
which are the same up to seven significant digits.

Fig. 12. Evolution of various energy components for the dynamic fracture problem in the PMMA strip with applied stretch $\epsilon_0 = 0.032$, and characteristic cohesive element size $h = 6.25$ μm.

4.1.4.3. Energy evolution. The evolution of various energy components for the spontaneous crack propagation simulation in the elastic strip with $\epsilon_0 = 0.032$ is shown in Fig. 12. During the dynamic simulation, some elastic energy U_{coh} is stored in the cohesive elements, which consists only of a nominal fraction of the total recoverable energy U. The total cohesive energy $\mathscr{E}_{coh}$ can be decomposed into recoverable elastic part U_{coh} and dissipated fracture energy $\mathscr{E}_{frac}$, and once the crack propagates through the entire strip, the fracture energy $\mathscr{E}_{frac}$ reaches a constant value.

Fig. 12 shows the total elastic energy U, kinetic energy K, energy dissipated by fracture $\mathscr{E}_{frac}$ and the sum of these terms. Energy conservation is verified as required. Apparently, the strain energy initially stored in the system gradually converts to fracture energy and drives the crack to propagate. A small portion of strain energy is converted to kinetic energy, which oscillates in equilibrium with the strain energy. If the strip is not pre-cracked, and no crack formation is allowed, then the energy components involved in the problem are the strain energy and the kinetic energy only. More strain energy is converted to the kinetic energy component.

4.1.4.4. Fracture energy required for crack propagating through strip. Since the cohesive elements are prescribed along a predefined path and at the end of simulation they are all debonded, the energy required for the entire fracture process can be evaluated analytically:

$$\mathscr{E}_{frac} = G_I A = 352.3 \text{ N m/m}^2 \times (1.9 \times 10^{-3} \text{ m} \times 1 \text{ m}) = 0.66935 \text{ N m},$$

while the finite element result is

$$\mathscr{E}_{frac}^{FEM} = 0.66944 \text{ N m},$$

which verifies (to a certain extent) the numerical implementation of cohesive elements.

The minimum initial stretch needed for the crack to propagate through the entire strip length can also be estimated. If kinetic energy (K) and elastic cohesive energy (U_{coh}) are neglected, i.e., assuming that all initial strain energy U_{bulk} (Eq. (35)) can be converted into fracture energy $\mathscr{E}_{\text{frac}}$, then $U_{\text{bulk}} \approx \mathscr{E}_{\text{frac}}$. Thus the initial stretch needed for crack propagating through the strip is obtained as $\epsilon_0 = 0.0301$. However, part of the initial strain energy is converted to kinetic energy (K) and elastic cohesive energy (U_{coh}). The elastic cohesive energy is nominal throughout the simulation, and we just estimate the kinetic energy. When the strip is stretched only along the y-direction at $t = 0$, the left and right boundaries of the strip are kept straight. Afterwards, these two boundaries tend to deform in a curved shape due to Poisson's ratio effect. The kinetic energy can be estimated as the difference in strain energy from initial deformation shape to this curved deformation shape, which is estimated numerically from Fig. 12 as $K = 0.05$ N m. Hence, the initial stretch needed for the crack to propagate through the entire strip is $\epsilon_0 \approx 0.0312$. This is consistent with the results shown in Fig. 9.

4.1.5. Crack propagation in an FGM strip

Now we consider an FGM strip with an initial crack and linear material property variation along the Cartesian direction x subjected to initial stretch as described in the homogeneous case. As explained previously, the graded element formulation approach is adopted in this study, and thus material properties are computed at nodal points and interpolated to Gauss points of elements. This concept also holds for cohesive elements. The detailed material properties are provided in Table 3. Young's modulus is three times as high at left side (4.86 GPa) as the right side (1.62 GPa), and the average Young's modulus is kept the same as the homogeneous PMMA strip. Poisson's ratio and material density are assumed to remain constant. The cohesive strength is kept as $T_{\max}(x) = E(x)/10$ and thus varies linearly along the x-direction. For the sake of simplicity, the critical interface separation is kept constant at the level $\delta = 0.4$ μm. The cohesive elements are again inserted along the ligament on the half-height plane ($a < x < L$, $y = H$), where $a = 0.1$ mm (same as before). For the current problem, Mode I fracture dominates, and the two FGM cohesive zone models discussed in Sections 3.1 and 3.2 will produce the same results. The necessary parameters for the effective quantity model (described in Section 3.1) are chosen as

$$\beta_1 = \beta_2 = 1, \quad \eta = \sqrt{2}.$$

Table 3
Material properties for linearly graded FGM strip subjected to initial stretch

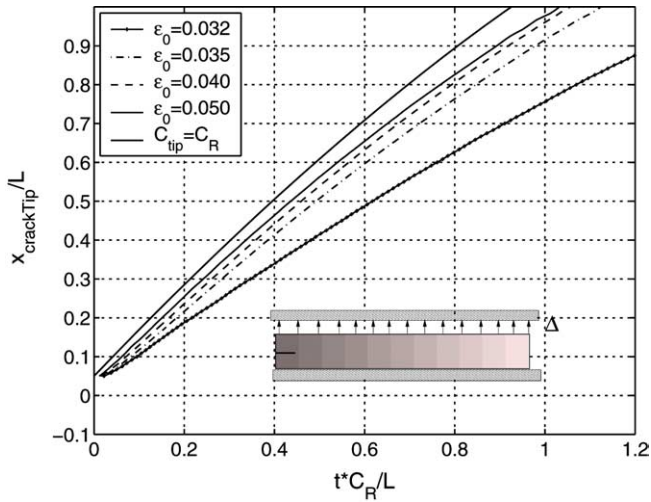| Location	E (GPa)	v	ρ (kg/m³)	G_{Ic} (N/m)	$T_{\max}$ (MPa)	δ (μm)
$x = 0$	4.86	0.35	1190	528.4	486	0.4
$x = L$	1.62	0.35	1190	176.1	162	0.4
Average	3.24	0.35	1190	352.3	324	0.4

Fig. 13. Normalized crack tip location versus normalized time for FGM strip subjected to various initial stretches (ϵ_0). Notice that, as expected, the Rayleigh wave speed varies along the Cartesian x direction.
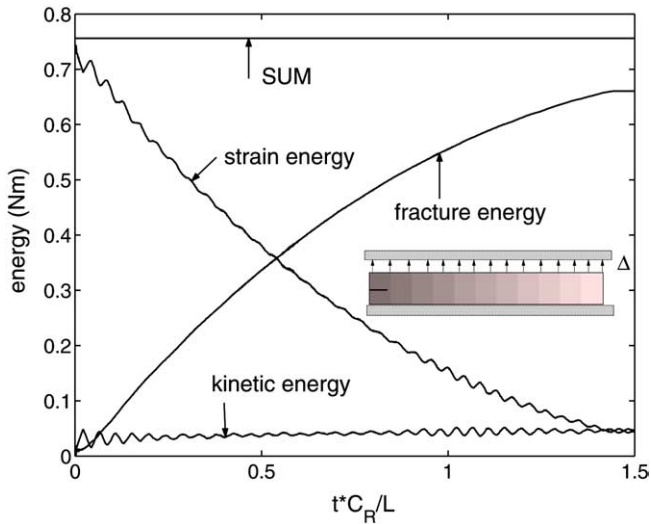

Fig. 14. Evolution of various energy components for the dynamic fracture problem in the FGM strip with applied stretch $\epsilon_0 = 0.032$, and characteristic cohesive element size $h = 6.25$ μm.

The stored strain energy drives the crack to propagate, and the numerical simulation results of crack tip location versus time for various ϵ_0 values are illustrated in Fig. 13.

Notice that the crack tip velocity is no longer constant, as in the previous example. This is due to the non-homogeneous material property. When the input energy is

sufficiently large, the crack tip velocity approaches the Rayleigh wave speed, which also depends on material location (i.e., $C_R = C_R(x)$). One observes that as the input energy increases, the crack tip velocity approaches the theoretical Rayleigh wave speed.

Again, energy balance is obtained, as illustrated in Fig. 14 for the initial stretch $\epsilon_0 = 0.032$. Notice that the fracture energy curve exhibits non-linear curvature (cf. Fig. 12). Obviously, the fracture energy required for the cohesive elements to lose cohesion is larger at left side than at right side, as indicated by the material property variation (Table 3).

First the numerical result of initial strain energy is checked with the theoretical value, which is computed according to expression (35) as

$$U_{\text{bulk}} = \frac{1}{2} \frac{3.24 \times 10^9}{1 - 0.35^2} 0.032^2 \times (4 \times 10^{-7}) = 0.756184615 \text{ N m}.$$

The numerical result is $U_{\text{bulk}}^{\text{FEM}} = 0.756184642$ N m, which agrees with the theoretical value up to seven digits (same agreement as before, with the homogeneous strip case). Note that the uniform stretch results in non-uniform stress field, hence the strain energy density also varies linearly along the x-direction, and the above formulation uses the average value of Young's modulus for simplicity.

The energy required for the crack to propagate through the strip is

$$\mathscr{E}_{\text{frac}} = \bar{G}_I A = 343.4 \times (1.9 \times 10^{-3}) = 0.65246 \text{ N m}$$

and the numerical result is

$$\mathscr{E}_{\text{frac}}^{\text{FEM}} = 0.65262 \text{ N m},$$

which agrees with the analytical value up to 3 digits. The energy release rate $\bar{G}_I$ in the above expression is the average value of G_I along $a \leqslant x \leqslant L$.

4.1.6. Spontaneous crack nucleation in an FGM strip

So far, the discussion in this section has been restricted to strips with an initial crack. For homogeneous material, a pre-crack is necessary for crack propagation to start. On the other hand, for FGM, since the material property is graded, uniform stretch results in non-uniform stress field, thus crack may nucleate at the region of relatively high stress and low cohesive strength, and thus crack may propagate spontaneously.

Consider an FGM strip with linear material variation along the Cartesian direction x, which is subjected to uniform stretch. The material properties are given in

Table 4
Material properties for FGM strip without pre-crack subjected to initial stretch

	E (GPa)	v	ρ (kg/m³)	δ (μm)	$T_{\max}^1$ (MPa)	$T_{\max}^2$ (MPa)	$T_{\max}^3$ (MPa)	$T_{\max}^4$ (MPa)
$x = 0$	4.86	0.35	1190	0.4	297	267	237	208
$x = L$	1.62	0.35	1190	0.4	297	267	237	208
Average	3.24	0.35	1190	0.4	297	267	237	208

Table 4. Young's modulus is three times as high at one side (4.86 GPa) as the other (1.62 GPa), and the average Young's modulus is the same as the homogeneous PMMA strip. The Poisson's ratio and material density remain constant. The critical interface separation is kept constant at the level $\delta = 0.4$ μm. Notice that multiple cohesive strength values (T_{max}^1 to T_{max}^4) are provided in Table 4. The reason will be discussed shortly. The cohesive elements are prescribed along the ligament on the half-height plane ($0 < x < L$, $y = H$), but without initial crack.

To nucleate a crack, the local stiffness, cohesive strength and stretch need to satisfy certain conditions, and the Poisson's ratio effect also plays a role. These issues are discussed next.

4.1.6.1. Critical stretch. In order to nucleate a crack with the CZM approach, the local stress must attain the level of the cohesive strength T_{max} to allow one or several nodes to experience debonding. Therefore, the material properties and the range of stretch values employed in previous sections cannot induce crack nucleation. For instance, provided the cohesive strength is $E(x)/10$, then the applied stretch $\epsilon_0 = 0.05$ cannot induce high enough local stress to form a crack. The relationship between local stiffness E, cohesive strength T_{max} and applied stretch ϵ_0 must reach roughly $\epsilon_0 \approx E/T_{max}$. After carrying out simulations for various T_{max} and ϵ_0 values, we conclude that at the critical value

$$\epsilon_0 \approx 0.82 \frac{E}{T_{max}} \tag{36}$$
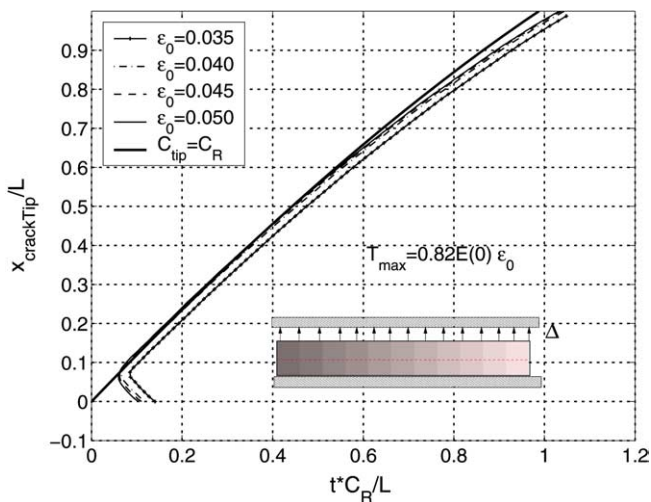

Fig. 15. Normalized crack tip location versus normalized time for FGM strip subjected to various initial stretches (ϵ_0) and T_{max}. The notation C_R denotes the Rayleigh wave speed, which varies along the horizontal direction.

crack nucleation will occur for the material system described in Table 4. Therefore, the cohesive strength T_{max}^1 to T_{max}^4 listed in Table 4 correspond to the following critical applied stretch: $\epsilon_0 = 0.05, 0.045, 0.04$ and 0.035, where E is taken as the value at the left side (4.86 GPa). The numerical simulation result of crack tip location versus time is illustrated in Fig. 15 for these four cases.

For the above material system, the FGM strip is stiffer at the left side ($E = 4.86$ GPa), and stress is proportional to material stiffness. Thus the stress is higher at the $x = 0$ vicinity, and crack initiates if Eq. (36) is satisfied. One observes from Fig. 15 that the crack initiation does not take place immediately. A short while after the simulation starts, the first nodal debonding occurs at $x = 0.07L$, i.e., not a boundary node. This is due to the Poisson's ratio effect, as will be discussed later. After this node is debonded, it serves as a crack nucleation location and the crack quickly runs in both directions, as shown by the turning of the curves in Fig. 15 at beginning stages. The crack tip location curve is not straight as in the homogeneous strip problem because, due to material non-homogeneity, the wave speed is varying along the x direction. The ideal case where the crack begins to propagate at $t = 0$ from the left edge with the Rayleigh wave speed is also plotted for reference. For the four cases discussed above, the crack tip velocities, i.e., the slope of the curves, differ marginally, and they are approaching the Rayleigh wave speed.

The energy evolution during the fracture process is investigated and the result for the case $\epsilon_0 = 0.35$ is plotted in Fig. 16. First the numerical result of initial strain energy is checked with the theoretical value, which is computed from expression (35), using the average value of Young's modulus, as follows:
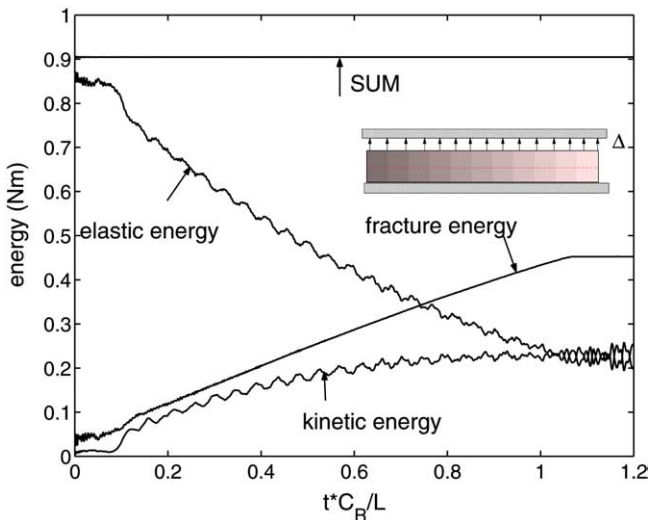

Fig. 16. Evolution of various energy components for the dynamic fracture problem in the FGM strip with applied stretch $\epsilon_0 = 0.035$, and characteristic cohesive element size $h = 6.25$ μm.

$$U_{\text{bulk}} = \frac{1}{2} \frac{3.24 \times 10^9}{1 - 0.35^2} 0.035^2 \times (4 \times 10^{-7}) = 0.904615385 \text{ N m}.$$

The numerical result is $U_{\text{bulk}}^{\text{FEM}} = 0.904615338$ N m, which agrees with the theoretical value up to seven digits.

The energy required for the crack to propagate through the strip is

$$\mathscr{E}_{\text{frac}} = \bar{G}_{\text{I}}A = \exp(1)T_{\max}\delta \times (2 \times 10^{-3}) = 0.452322 \text{ N m},$$

while the FEM result is

$$\mathscr{E}_{\text{frac}}^{\text{FEM}} = 0.452342 \text{ N m},$$

which agrees with the theoretical prediction up to 4 digits and energy conservation is again obtained. The curve denoting fracture energy evolution is almost a straight line because the cohesive strength is constant along the x-direction in this simulation, and the slight curvature is only introduced by the non-linear crack tip speed.

4.1.6.2. Poisson's ratio effect. For a one-dimensional problem, the coefficient in Eq. (36) would be 1 instead of 0.82. The reduction of critical stretch required for crack to nucleate in this problem is due to the Poisson's ratio effect. The initial condition dictates a uniform elongation in the Cartesian y-direction while all nodes are kept stationary in the x-direction. When the dynamic simulation starts, the nodes at left and right edges tend to vibrate along the x-direction due to the Poisson's ratio effect. This movement causes the nodes adjacent to them to move inside, yet those nodes are under constraint and cannot move freely. Therefore, interior nodes that are closer to the left edge endure larger stresses, and hence one of them debond first. Since this
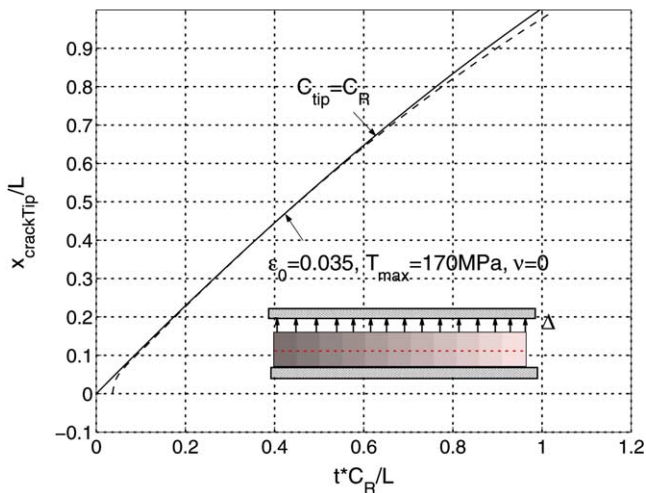

Fig. 17. Normalized crack tip location versus normalized time for FGM strip subjected to initial stretch ϵ_0. The Poisson's ratio is set to $v = 0$. Notice that the Rayleigh wave speed varies along the horizontal direction.

effect is caused by the Poisson's ratio effect, a test was performed to check if it vanishes with $v = 0$, which is described below.

Consider an FGM strip, which is subjected to initial stretch $\epsilon_0 = 0.035$, with the same material properties as described in Table 4, except for the Poisson's ratio, which is set to be $v = 0$. The boundary conditions are the same as in the previous example problem. The cohesive strength corresponding to the critical stretch is calculated as $T_{max} = E(x = 0) \times \epsilon_0 = 170$ MPa. The numerical simulation result of crack tip location versus time is illustrated in Fig. 17. As expected, the first debonded node is the boundary node, and the crack quickly propagates through the strip. Notice that the average Rayleigh wave speed is $C_R = 1020$ m/s when $v = 0$.
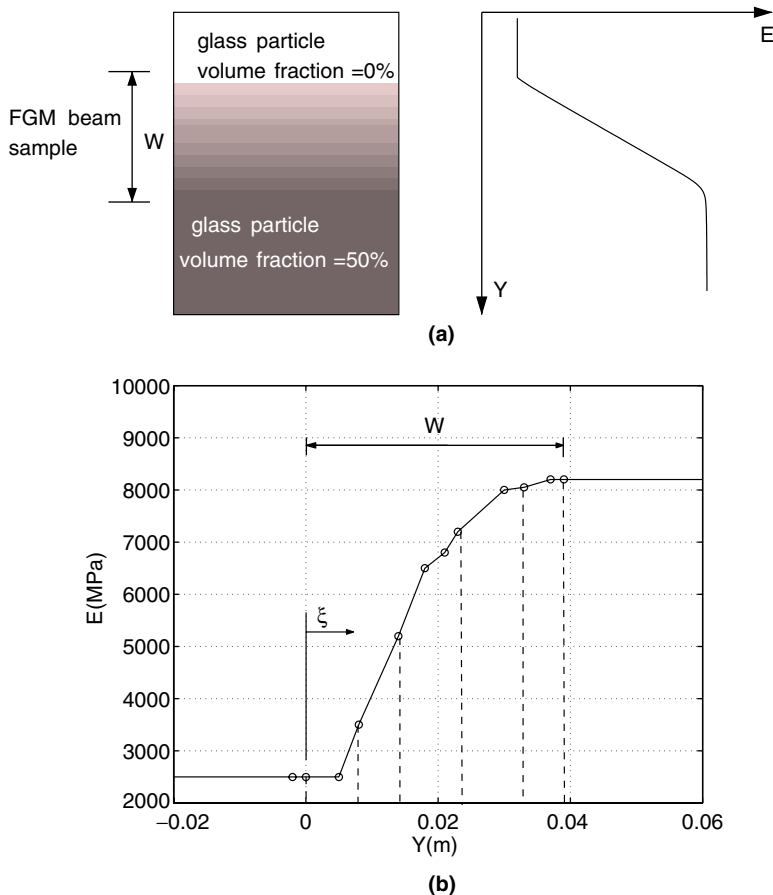

Fig. 18. Material gradation and Young's modulus variation of glass/epoxy FGM: (a) schematic representation of glass particles volume fraction distribution and modulus variation in FGM plate and (b) experimental data of Young's modulus variation in FGM beam. Discrete data points retrieved from Figure 1 of Rousseau and Tippur (2000), representing experimentally evaluated Young's modulus at normalized length $\xi = Y/W = 0, 0.17, 0.33, 0.58, 0.83$ and 1.

4.2. Dynamic fracture of epoxy/glass FGM beams under impact loading

The FEM scheme incorporating graded bulk and cohesive elements was verified in the previous section, with emphasis on mesh convergence, mesh orientation and energy balance. Equipped with this knowledge, we proceed to investigate a real FGM fracture problem. To date experimental data of real FGMs subjected to dynamic loading are rare. Rousseau and Tippur (2000, 2001a,b, 2002a,b) have conducted some pioneering work on dynamic experiments of polymer-based FGMs. In the present study, numerical simulations of the specimens investigated by Rousseau and Tippur (2001a) are carried out in conjunction with the present cohesive model approach, which leads to further insight into the dynamic fracture behavior of FGMs.

The FGMs under test were epoxy/glass materials, with epoxy as matrix and glass particles dispersed in the matrix. In the manufacturing process, glass particles of mean diameter 42 μm were dispersed into epoxy matrix, and due to higher mass density (ρ_{glass} = 2470 kg/m^3, ρ_{epoxy} = 1150 kg/m^3), glass particles sank gradually into the slowly curing matrix, and finally a smooth distribution of monotonically increasing (from top to bottom) volume fraction of glass spheres was formed (Fig. 18(a)). Experiments on both monolithic (with uniform volume fraction of particle inclusion in the material) and FGM specimens under dynamic loading were carried out. Rousseau and Tippur (2002b) reported material property change under dynamic load, investigated stress fringe patterns and stress intensity factors for both crack along and perpendicular to material gradation. Standard finite element simulation was carried out using ABAQUS to predict crack initiation time, and the conclusion was drawn that crack initiates earlier for a beam softer at the cracked side than a beam stiffer at the cracked side (Rousseau and Tippur, 2001b). In this section, numerical simulations of Rousseau and Tippur's experiments are performed, and results turn out to be consistent with their predictions.
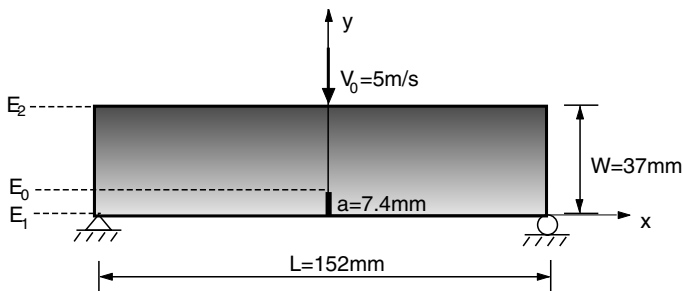

Fig. 19. Geometry, load and boundary conditions for epoxy/glass beam under low velocity impact loading. The parameters E_0, E_1 and E_2 denote Young's modulus at the crack tip, bottom surface and top surface, respectively.

Table 5
Material properties of three-point bending FGM specimen, obtained from Rousseau and Tippur (2001a)

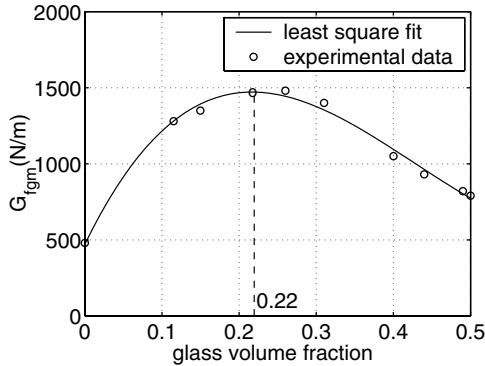| V_f	E (GPa)	v	ρ (kg/m^3)
0	4.74	0.35	1150
0.5	10.74	0.30	1810

Fig. 20. Cohesive energy of epoxy/glass FGM versus volume fraction of glass particle inclusion. Experimental data are retrieved from the paper by Rousseau and Tippur (2000, Fig. 3), and the smooth curve is obtained by least square fitting of experimental data.

4.2.1. Problem description

The geometry and boundary conditions are depicted in Fig. 19. An FGM beam is subjected to low velocity (5 m/s) impact loading, which is applied at the center point of the top surface. Material gradation is along the Cartesian y-direction, and an initial crack of length $a = 0.2W = 7.4$ mm is predefined at the center of the bottom face of the beam.

The epoxy/glass FGM is manufactured such that it possesses a smooth transition profile of volume fraction of glass spheres (V_f) varying from 0% at one side to 50% at the other, and in between the V_f variation is approximately linear. The material properties with volume fraction $V_f = 0$ and $V_f = 0.5$ are listed in Table 5.

The cohesive energy is non-linear with respect to glass inclusion volume fraction and is plotted in Fig. 20. The critical energy release rate data were obtained by conducting 3-point-bending test on monolithic glass/epoxy specimen of different volume fraction of glass inclusions (Rousseau and Tippur, 2002a). Fig. 20 shows that the cohesive energy curve attains maximum value at volume fraction of glass inclusion around 22%, rather than at the maximum glass inclusion volume fraction of 50%. A comparison of the model described in Section 3.1 with the experimental result by Rousseau and Tippur (2000) reveals that in the former, the energy grows monotonically as volume fraction of metal phase increases; while, in the latter, it increases at small volume fraction of glass inclusion, and then decreases gradually when the volume fraction of inclusion exceeds 22%. Rousseau and Tippur (2001a) explained

that the underlying mechanism for this interesting phenomena is due to the fact that the strength of glass is much higher than that of epoxy, and thus the crack develops along the interfaces between the two phases rather than penetrating the glass particles. Therefore, the presence of glass inclusion makes the crack path tortuous, and results in greater crack surface area, hence larger fracture resistance. On the other hand, however, at higher volume fraction, the glass particles tend to agglomerate and form local defects. Thus the toughness becomes a competition of the two mechanisms, and as glass volume fraction increases, the toughness first increases, attains its maximum value, and then it drops gradually.

To investigate the influence of material variation on crack initiation and propagation features, five sets of material properties of different gradation profiles were used in the simulation:

1. FGM: crack is located on the compliant side, i.e., if we designate subscript 1 to indicate bottom surface and 2 top surface, then $E_2 > E_1$, and the specimen is impacted on the stiffer side.
2. FGM: $E_2 < E_1$, crack is located on the stiffer side, and impacted at the more compliant side.
3. Homogeneous: $V_f = 0.1$, i.e., $E_1 = E_2 =$ Young's modulus E_0 at crack tip in case 1.
4. Homogeneous: $V_f = 0.4$, i.e., $E_1 = E_2 =$ Young's modulus E_0 at crack tip in case 2.
5. Homogeneous: $V_f = 0.25$, i.e., $E_1 = E_2 =$ median value of Young's modulus in case 1 and 2.

In the last three cases, the material under investigation is a composite, which is essentially a monolithic specimen with uniform volume fraction of each phase. For the sake of convenience, this ''macroscopically uniform'' material specimen is referred to as ''homogeneous'' from now on.

4.2.2. Effective material property

Under dynamic load, material behaves stiffer than in static case. Experimental data for FGM properties under quasi-static and dynamic load are given in Rousseau and Tippur (2000, 2001b), respectively. Under static load, Young's modulus variation is between range $E = 2.6$ GPa at $V_f = 0$ to $E = 8$ GPa at $V_f = 0.5$ (the numbers are read from Rousseau and Tippur (2000, Fig. 1)), while under dynamic load, Young's modulus varies from $E = 4.5$ GPa at $V_f = 0$ to $E = 11$ GPa at $V_f = 0.5$ (the numbers are read from Rousseau and Tippur (2001b, Fig. 5)). The variation in Poisson's ratio was not reported, and presumably it would be within a moderate range that would not affect the results noticeably. Thus v is assumed to be the same as in the static case. As for the mass density ρ, it is regarded as constant whether under static or dynamic loading. Due to emphasis of this work on dynamic analysis, the material property under dynamic load is used.

Multiple theories exist to estimate effective properties of typical epoxy/glass composites. In the present study, the Mori–Tanaka method is employed. Rousseau and Tippur (2002a) have reported good agreement between this estimation and experimental results for the static case, and here we assume that this method also gives

acceptable estimation of material properties under dynamic load. To obtain the effective property at nodal points, first the volume fraction of glass phase (V_f) is calculated at each node. Next, the bulk modulus κ and the shear modulus μ of the composite are computed:

$$\kappa = \kappa_m \left[1 + \frac{V_f}{\frac{3(1-V_f)\kappa_m}{3\kappa_m+4\mu_m} + \frac{\kappa_m}{\kappa_i-\kappa_m}} \right], \tag{37}$$

$$\mu = \mu_m \left[1 + \frac{V_f}{\frac{6(1-V_f)(\kappa_m+2\mu_m)}{5(3\kappa_m+4\mu_m)} + \frac{\mu_m}{\mu_i-\mu_m}} \right], \tag{38}$$

where the subscripts m and i denotes the matrix and the inclusions, respectively, and

$$\kappa_m = \frac{E_m}{3(1-2v_m)}, \quad \mu_m = \frac{E_m}{2(1+v_m)}; \quad \kappa_i = \frac{E_i}{3(1-2v_i)}, \quad \mu_i = \frac{E_i}{2(1+v_i)}. \tag{39}$$

Thus the effective Young's modulus and Poisson's ratio are given by (see, Nemat-Nasser and Hori, 1993; Soboyejo, 2003):

$$E_{eff} = \frac{9\mu \times \kappa}{\mu + 3\kappa}, \quad v_{eff} = \frac{1.5\kappa - \mu}{\mu + 3\kappa}. \tag{40}$$

Effective material properties versus volume fraction of glass sphere inclusion V_f are plotted in Fig. 21. In the current computation, V_f is assumed to vary linearly in the FGM gradation direction. Therefore, Fig. 21 effectively shows the material property gradation profile in the FGM beam along the Cartesian y-direction.
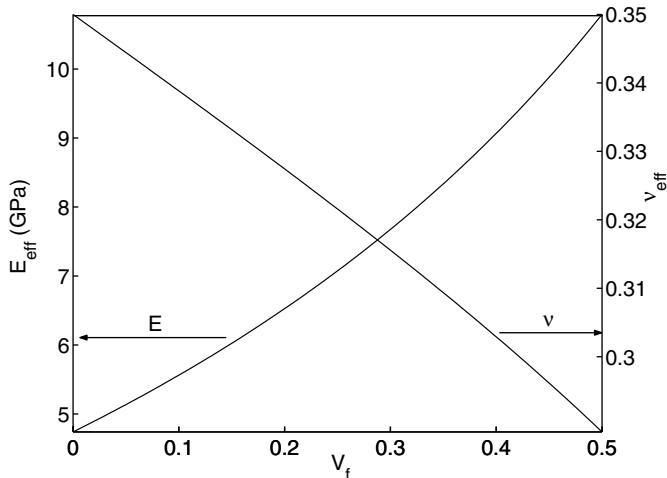

Fig. 21. Effective Young's modulus (E_{eff}) and Poisson's ratio (v_{eff}) versus volume fraction of glass sphere inclusion.
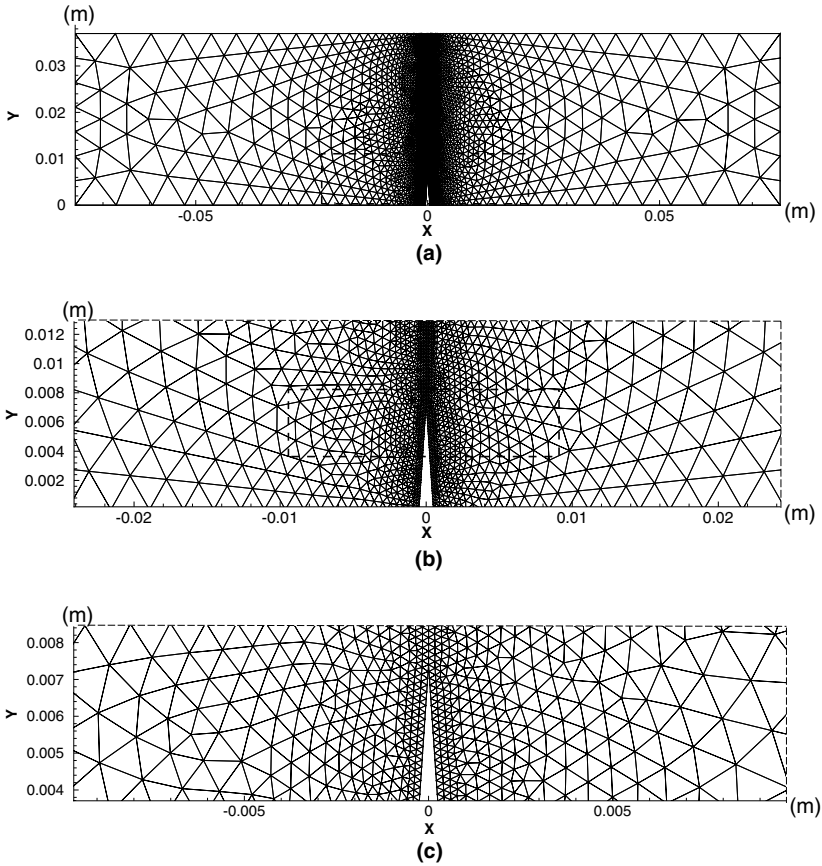
Fig. 22. Mesh for three-point bending beam subjected to impact loading. Mesh contains 14,991 nodes before cohesive elements are generated, 15,312 nodes after cohesive elements are generated, 7388 T6 elements and 160 cohesive elements. Uniform cohesive element size equals $2h = 185$ μm: (a) global mesh, (b) zoom of block region in (a) and (c) zoom of block region in (b).

4.2.3. Discontinuity issues

T6 elements are used in the bulk discretization, and the mesh is illustrated in Fig. 22. Cohesive elements are prescribed along the path at $x = 0$ (the symmetry line), so that the crack will propagate along the defined path.

Based on the discussion in the previous Section, the choice of cohesive element size should take into account the cohesive zone size ℓ_k (Eq. (32)) as well as the maximum cohesive strength T_{max} and the critical opening displacement δ. A high cohesive strength, e.g., $E/T_{max} = 10$ would result in a shorter cohesive zone size, and thus induce a more stringent element size requirement. In this problem, $E/T_{max} = 10$ gives cohesive zone size of approximately 15.5 μm. Notice that due to non-homogeneous material property, the determination of ℓ_k is based on sampling at a number of

points of different volume fraction (V_f) of glass inclusion, and then the smallest ℓ_k is chosen, which occurs at $V_f = 0.50$, the stiffest edge. According to the convergence requirement (Geubelle and Baylor, 1998; Klein et al., 2000), the element size should be at most 1/2 to 1/3 of the cohesive zone size, so this estimation gives element size of at most 8 μm, which leads to a very large number of nodes and elements, hence heavy computation load. However, since cohesive elements are inserted only along a defined line, we can assume that using a lower T_{max} value would not add too much compliance to the structure. The elastic compliance added to the structure can be estimated similarly to (Zavattieri and Espinosa, 2001) – see also (Baylor, 1998; Klein et al., 2000):

$$E_{add} = \frac{T_{max}}{\delta} \times b_s = \frac{E/50}{0.4 \times 10^{-6}} \times 76 \times 10^{-3} = 3800E,$$

where b_s is taken as half of the beam specimen length. The ratio of structural compliances before and after cohesive element insertion is thus estimated to be 1:1/(1 + 1/3800) = 1:1.0003. Therefore, $E/T_{max} = 50$ is used, which results in $\ell_k = 387$ μm. The element size shown in Fig. 22 refers to $2h = 185$ μm, so the cohesive zone spans at least 2 cohesive elements, which is roughly within the convergence requirement.

If an insufficiently refined mesh is used, which violates the convergence rule, then a crack appears ahead of the main crack front. For example, when the $E/T_{max} = 10$ ratio is used, and the element size held at $2h = 185$ μm, which is much larger than cohesive zone size $\ell_k = 26.6$ μm, the crack pattern illustrated in Fig. 23 is obtained. As can be seen in this plot, before the crack tip node experiences complete
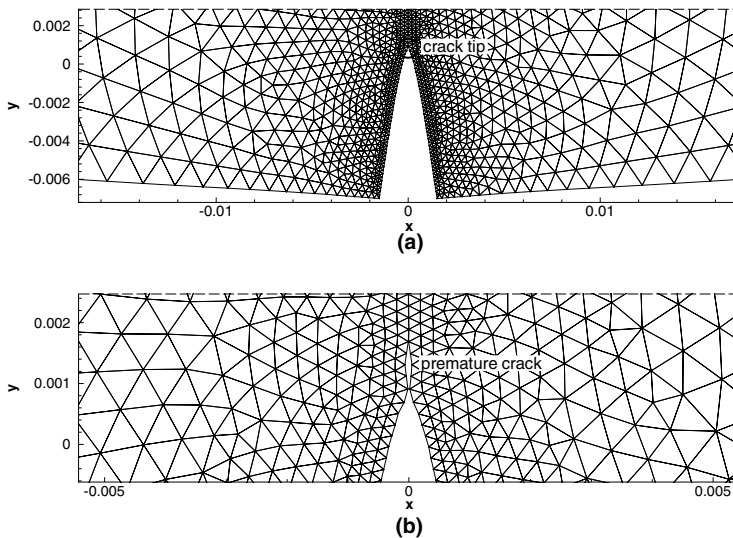

Fig. 23. Premature crack front for FGM beam under dynamic load (Fig. 19).

Table 6
Material properties and crack initiation time for three-point bending homogeneous beam

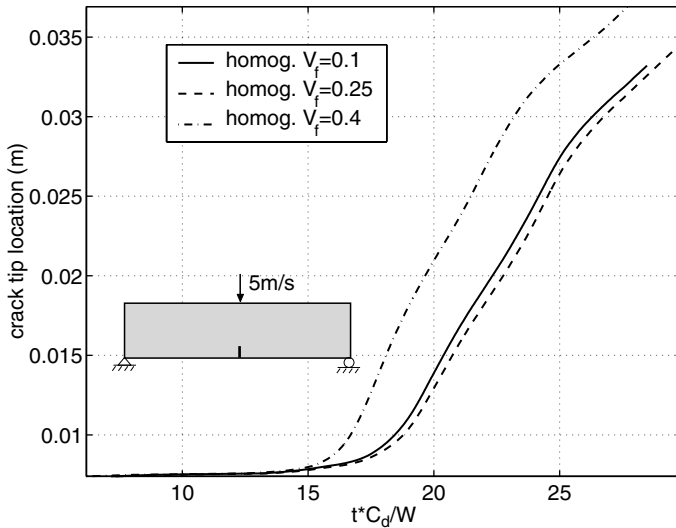| V_f	E (GPa)	v	ρ (kg/m^3)	C_d (m/s)	G_{Ic} (N/m)	T_{max} (MPa)	δ (μm)	ℓ_k (μm)	h (μm)	t_i (μs)	t_i^*
0.10	5.517	0.3406	1282	2218	1175.3	110.3	3.92	1166	92.5	120	7.2
0.25	7.020	0.3257	1480	2327	1459.6	140.4	3.82	1136	92.5	117	7.4
0.40	9.010	0.3103	1678	2476	1101.8	180.2	2.25	666	92.5	92	6.2

Fig. 24. Crack tip location versus normalized time for homogeneous beams with V_f=0.1, 0.25 and 0.4; Dilatational wave speed C_d = 2218, 2317 and 2476 m/s for beams with $V_f = 0.1$, $V_f = 0.25$ and $V_f = 0.4$, respectively.

decohesion, some other nodes ahead are separated. This undesirable effect, however, can be avoided by careful control of the cohesive element size.

4.2.4. Results

First, results for the three homogeneous beams of Section 4.2.1 are presented. Table 6 gives the material properties and crack initiation time for these three cases. The crack tip location with respect to normalized time is plotted in Fig. 24. The dilatational wave speed C_d is defined by Eq. (11) with constant material properties (E, ρ, v) for plane stress case. The times t_i and t_i^* denote crack initiation time in absolute scale (seconds) and normalized scale ($t_i \times C_d/W$, where W is the height of the beam), respectively.

On an absolute time scale, the stiffer the material, the earlier the crack starts to propagate (i.e., $t_i^{(V_f=0.4)} < t_i^{(V_f=0.25)} < t_i^{(V_f=0.1)}$, cf. Table 6). Three factors are attributed to this observation. First, in a stiffer media, waves propagate faster, and stress concentration accumulates at a higher speed, so that the crack tends to grow earlier than in the softer media. Fig. 24 uses normalized time, thus the influence of different wave

speed is partly excluded. The normalization changes the relative position of the curves corresponding to $V_f = 0.1$ and $V_f = 0.25$. Second, for linear elasticity problem, the force applied and the stress induced are proportional to the specimen stiffness when displacement loading is prescribed. This effect is also present here although the problem under investigation clearly exhibits non-linearity through the cohesive model. Third, the material resistance capacity against fracture, represented by the cohesive energy shown in Fig. 20 for material with different glass volume fraction, controls the crack initiation and propagation behavior. Notice that the sequence of crack initiation times normalized with respect to the average dilatational wave speed is the same as the order of fracture energy (i.e., $t_i^{*(V_f=0.4)} < t_i^{*(V_f=0.1)} < t_i^{*(V_f=0.25)}$, cf. Table 6). Since the local maximum cohesive strength T_{max} is assumed to be proportional to the local Young's modulus ($E/T_{max} = 50$), the stiffer material gives higher T_{max} value. Although this seems to enhance the resistance of local material against crack initiation, it also causes the critical separation δ to decrease, since the exponential cohesive law states cohesive energy $G_{Ic} = eT_{max}\delta$. All these factors are combined to produce the crack initiation and propagation behaviors shown in Fig. 24.

After crack initiation, the crack tip appears to remain at a "plateau" status for around 130 μm, during which the crack front advances very little. After careful examination of the deformation shape of the beam, we can explain the "plateau stage" as follows: when impact load is applied on the top surface of the beam, first a compressive stress wave propagates downwards, then reflects at the bottom surface, and propagates upward as tensile wave. During the same time, since velocity is imposed continuously, the subsequent waves also propagate downwards and reflect. After a short while, the combined effect of superimposed waves that propagate back and forth become rather complicated, and at the crack tip, the σ_x stress, which is the primary driver for crack extension, does not necessarily increase monotonically. In fact, it can be observed that the crack mouth opening displacement (CMOD) first increases, then decreases, and increases again during certain phase of the simulation. At an early stage, when the stress at the initial crack tip attains critical value, one pair of nodes break up, then it takes another time interval for the stress to arrive at an equally high level to break up the next pair of nodes. This is the "plateau" stage. However, in the long run, the bending effect predominates over the wave effect and local deformation at the crack tip monotonically increases, and thus the crack propagates at a much faster velocity.

Table 7
Material properties and crack initiation time for three-point bending homogeneous and FGM beams

| Material	E (GPa)	v	ρ (kg/m^3)	C_d (m/s)	G_{Ic} (N/m)	T_{max} (MPa)	δ (μm)	t_i (μs)	t_i^*	$t_i^{\text{Experiment a}}$
$V_f = 0.10$	5.517	0.3406	1282	2218	1175.3	110.3	3.92	120	7.2	–
$V_f = 0.25$	7.020	0.3257	1480	2327	1459.6	140.4	3.82	117	7.4	–
$V_f = 0.40$	9.010	0.3103	1678	2476	1101.8	180.2	2.25	92	6.2	–
FGM:$E_2 > E_1$	7.292	0.3252	1480	2308	1166.2	145.8	2.94	101.5	6.3	6.0–6.4
FGM:$E_2 < E_1$	7.292	0.3252	1480	2308	1166.2	145.8	2.94	113.4	7.1	7.0–7.4

[a] Experimental results from Rousseau and Tippur (2001a).
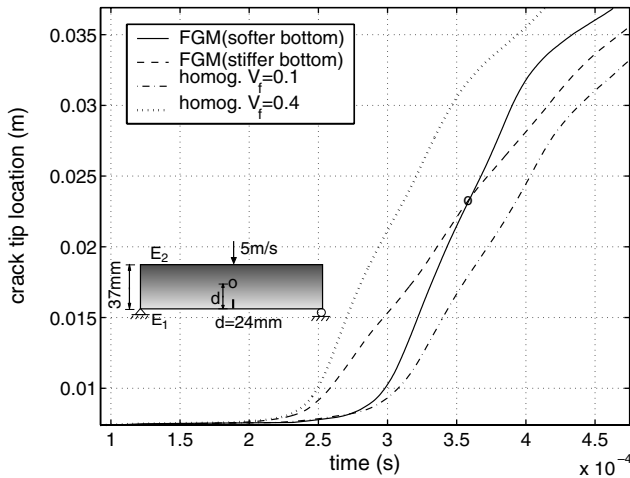
Fig. 25. Crack tip location versus time for two FGM beams and two homogeneous beams with $V_f = 0.1$ and 0.4. V_f denotes volume fraction of glass inclusion in specimen material. The intersection point of the two curves for FGM beams is indicated with a circle on the curves and also on the insert (beam figure).

When the crack speeds up, it propagates smoothly to the top surface. Crack extension evaluated at the normalized time (Fig. 24(b)) also reveals that fracture energy controls the crack propagation: the crack propagates slowest for the specimen with highest fracture energy (1459.6 N/m for $V_f = 0.25$ versus 1175.3 N/m for $V_f = 0.10$ and 1101.8 N/m for $V_f = 0.40$).

Next we proceed to investigate the influence of material gradation. The relevant material properties and crack initiation time are listed in Table 7.

The crack tip location with respect to time is plotted in Fig. 25 and the following observations can be made:

- The crack tip location profiles of the FGM beams are bounded between results for the two homogeneous cases.
- For $E_2 > E_1$ case (the beam is more compliant at cracked surface), crack initiates at $t = 101.5$ μs; for $E_2 < E_1$ case (the beam is stiffer at cracked surface), crack initiates at $t = 113.4$ μs. This trend is consistent with the prediction made by Rousseau and Tippur (2000). However, this is different from the homogeneous cases, for which crack initiates earlier in the stiffer material.
- After the first node experiences decohesion, both cases experience a time interval during which the crack extends slowly. It is relatively longer for the $E_2 > E_1$ case, with a "plateau" time of around 170 μs, and shorter for the $E_2 > E_1$ case, with a "plateau" time of around 110 μs.
- After the crack propagation speed up, at first the crack tip of beam with $E_2 > E_1$ is ahead of that of the beam with opposite material gradation ($E_2 < E_1$), as illustrated in the stress field σ_x plot in Fig. 26. However, the crack tip in the $E_2 < E_1$ case accelerates faster than the other, and at time around 360 μs, the crack
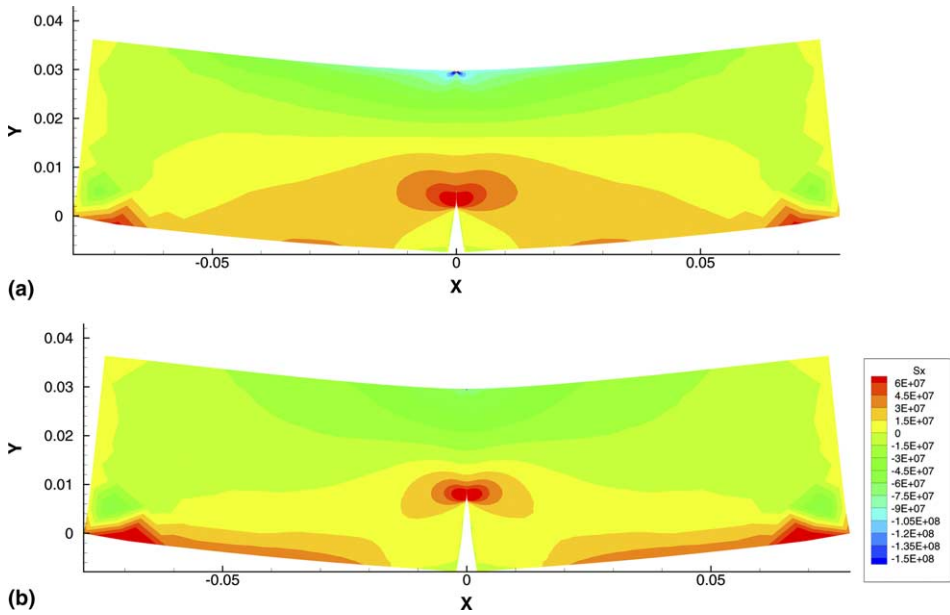
Fig. 26. Comparison of stress field σ_x (units: Pa) at $t = 300$ μs for FGM beams subjected to three-point bending; (a) beam softer at bottom ($E_2 > E_1$); (b) beam stiffer at bottom ($E_2 < E_1$).

tips in both cases reach the same crack tip location (represented by the crossing of curves in Fig. 25), and afterwards the one in the $E_2 < E_1$ case keeps advancing ahead of the other one.

• Comparison of crack propagation time between experiments (Rousseau and Tippur, 2002a) and numerical simulation shows good agreement (Table 7). The normalized crack initiation time $t_i^* = t \times C_d/W$ from the experiment (Rousseau and Tippur, 2001a) is within the range 6.0–6.4 for the compliant-bottom beam ($E_2 > E_1$) and 7.0–7.4 for the stiff-bottom beam ($E_2 < E_1$), respectively, while the numerical simulation results are 6.3 and 7.1, respectively. However, the experiment does not observe a significant "plateau" stage after crack initiation. This may be understood as the artificial compliance effect due to the cohesive law adopted in the simulation. The presence of cohesive elements in the mesh before the numerical simulation starts inevitably introduces artificial compliance to the structure. By using initially rigid cohesive model, this effect can be eliminated. Another difference in the experiment setting and the numerical simulation is associated with the crack tip modeling. In the experiment, the crack tip is a 150 μm sized notch, while the simulation assumes initially sharp crack. This may suggest more singular stress fields for the numerical simulation compared to the experiment. However, during the simulation, the cohesive elements located at the crack tip region respond to the finite tensile stress with opening displacement before the
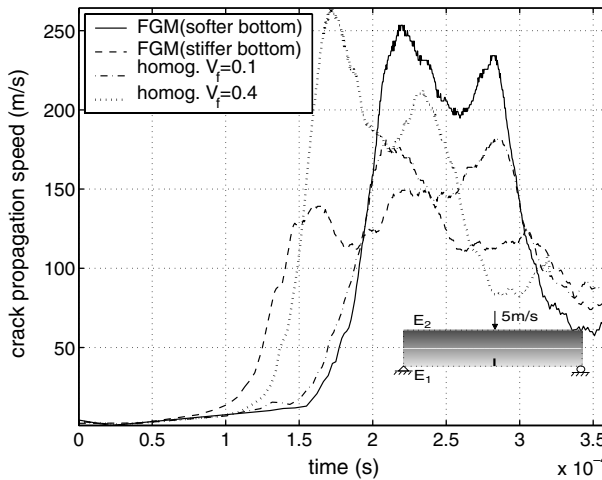
Fig. 27. Crack tip velocity versus $t - t_i$ for for two FGM beams and two homogeneous beams with $V_f = 0.1$ and 0.4, where t_i denotes crack initiation time.

elements suffer complete separation (no load bearing capacity). Therefore singularity is not activated at the crack tip. Thus this issue may not be a major contributing factor for the "plateau" stage in the simulation.

The comparison of velocities of both FGM and homogeneous beams can be clearly observed in Fig. 27, which shows the crack extension speed versus time. For the sake of clarity, the time axis is shifted by $t - t_i$, in which t_i denotes crack initiation time. Two factors contribute to the crack propagation speed: local stress σ_x, which is the primary driving force of crack extension; and fracture resistance. For the homogeneous beams, the difference in fracture energy and the higher stress associated with higher stiffness are the main causes of the different crack propagation speeds. Therefore, the crack advances faster in the $V_f = 0.4$ beam than in the $V_f = 0.1$ beam. On the other hand, although the average stiffness and fracture energy are the same for the two FGM beams (see Table 7), the crack speeds are much different. In the softer bottom beam, after crack propagation picks up speed (during the time range 200–300 µs), the crack propagates faster than the stiffer bottom beam. This can be understood as follows: in FGM beams, shift of the neutral axis position from the geometrical center introduces a significant stress difference at the crack tip, compared to the homogeneous case. For instance, for a softer-bottom beam ($E_2 > E_1$), the neutral axis is shifted towards the upper surface compared to the homogeneous beam, leading to a longer distance measured from the neutral axis to the crack tip location, denoted as y_c. Since the crack tip stress is positively related to y_c for bending problem (for a static pure bending problem $\sigma_x = M y_c / I$ in which M and I denote bending moment and the second moment of area, respectively), the shift results in higher stress value at the crack tip for the softer-bottom beam ($E_2 > E_1$) compared to a homogeneous beam under same loading condition. This trend is reversed for

the stiffer-bottom beam ($E_2 < E_1$). Apparently, higher stress level tends to accelerate the crack extension speed, and the crack propagates faster in the softer-bottom beam case than the stiffer-bottom beam case. Without overlooking the other factors influencing crack speed, e.g., local fracture resistance and reflective stress waves, we emphasize the importance of material gradation by inducing neutral axis shift on the crack propagation behavior in the bending beam problem.

The stress field σ_x plots for the two FGM beams at time $t = 300$ μs are shown in Fig. 26. Clearly, the crack tip location is more advanced in the beam with $E_2 < E_1$ (stiffer bottom) than in the beam with $E_2 > E_1$ (softer bottom) at this time instant. To further illustrate the difference of crack evolution pattern in the two FGM beams,
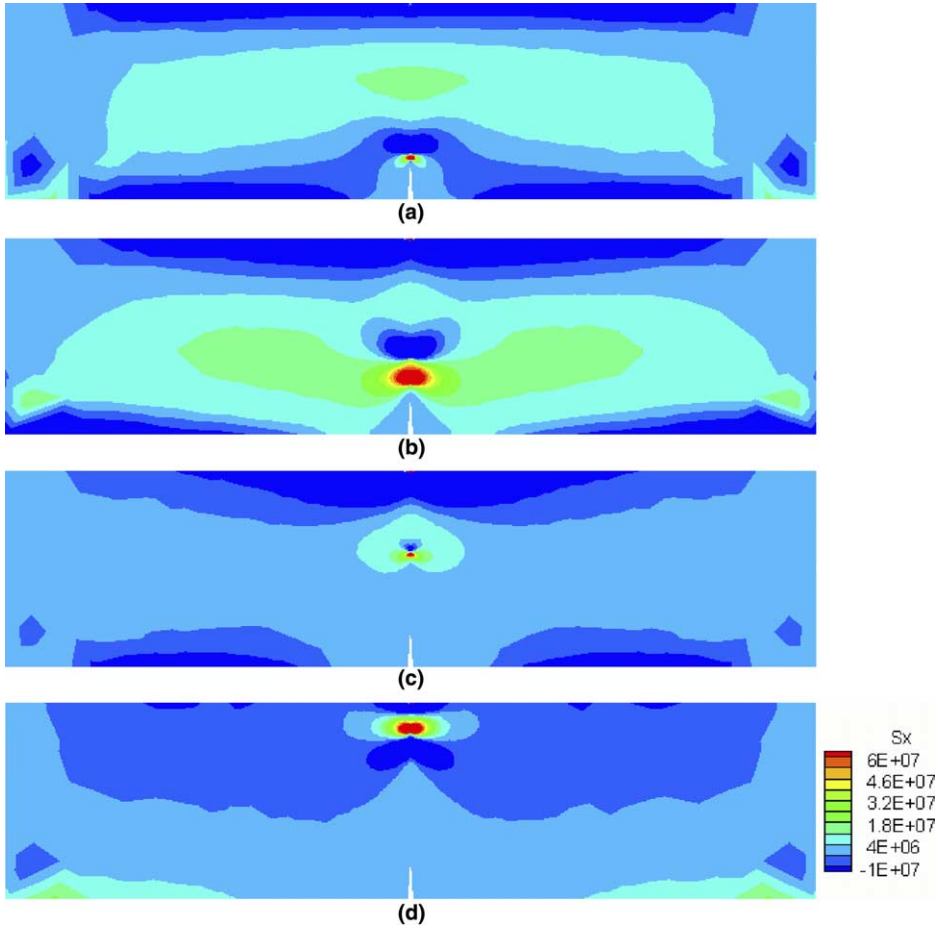

Fig. 28. Difference in value of stress field $\sigma_x^{\text{softbottom}} - \sigma_x^{\text{stiffbottom}}$ (units: Pa) for three-point bending FGM beam at different times: (a) $t = 250$ μs, crack tip of the stiffer-bottom beam begins to take speed, (b) $t = 300$ μs, both cracks speed up, crack tip of softer-bottom beam is below that of stiffer-bottom beam, (c) $t = 350$ μs, crack tip of softer-bottom beam catches up with that of the stiffer-bottom beam and (d) $t = 400$ μs, crack tip of softer-bottom beam overtakes that of the stiffer-bottom beam.

the difference of stress field σ_x for the two FGM specimens, calculated as $\sigma_x^{\text{softer bottom}} - \sigma_x^{\text{stiffer bottom}}$, is plotted in Fig. 28, in the undeformed configuration. The positive values, represented by contours of red color, indicate regions where the stress of softer-bottom beam is higher compared to stiffer-bottom at certain time instant, while the negative values, represented by contours of blue color, indicate the reverse situation. Since the peak values for each case occur at the crack tips, the centers of the red and blue contours indicate the crack tips of the softer-bottom beam and stiffer-bottom beam, respectively. Apparently, first the crack tip of the stiffer-bottom beam advances ahead of the softer-bottom beam, but the situation reverses at around $t = 360$ μs and height 24mm.

4.3. Mixed-mode dynamic crack propagation

The two examples in Sections 4.1 and 4.2 illustrate the application and versatility of the CZM approach in dynamic fracture simulations for homogeneous and graded materials. In both examples, the fracture paths are predefined and the crack grows in Mode I only. This section is devoted to study mixed-mode dynamic fracture.

A clear understanding of physical mechanisms governing the dynamic crack propagation under mixed-mode loading remains elusive. General observation drawn primarily from quasi-static analysis indicate that under mixed-mode loading, the existing crack tends to grow according to the local Mode-I condition, e.g., in the direction of maximum hoop stress at the immediate vicinity of the crack tip. Another widely adopted fracture criterion in quasi-static crack propagation analysis is based on energy consideration, in which the crack tries to find the path of least resistance and thus maximize the energy release rate (Anderson, 1995). These approaches re-
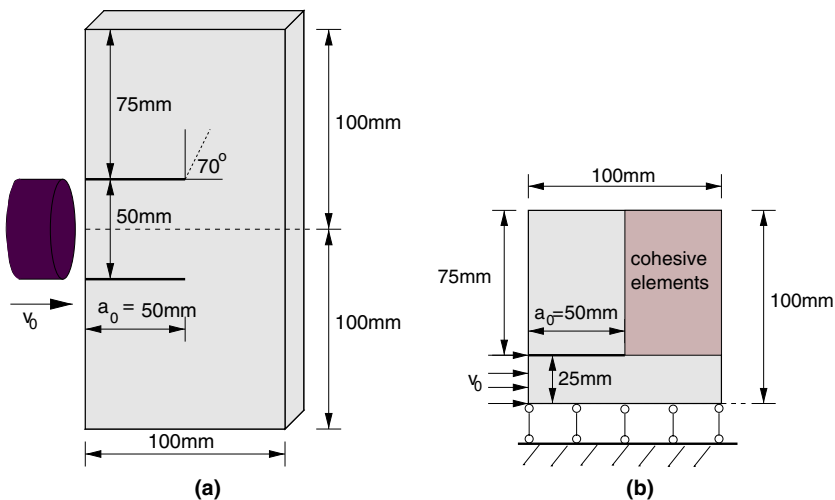

Fig. 29. (a) Geometry and loading of the Kalthoff–Winkler experiments Kalthoff and Winkler (1987); (b) 2-D plane-strain FEM simulation model.

quire evaluation of external fracture criterion during simulation. In this section, the cohesive zone model is employed to study a mixed-mode dynamic crack propagation problem, where the cohesive elements allow crack initiation and turning of crack paths to occur spontaneously without predefining crack path nor prescribing a separate fracture criterion.

4.3.1. Kalthoff–Winkler experiments

Kalthoff and Winkler (1987) tested specimens, as shown in Fig. 29(a), where a plate with two edge notches is subjected to an impact by a projectile. The two notches extend to around half plate width. The experiments demonstrated different fracture/damage behaviors of a maraging steel material under various loading rates. Depending on the loading rate v_0 and notch tip radius r_0, the crack tip experiences different stress intensity factor rate. At lower strain rate factor v_0/r_0, brittle fracture occurs with a propagation angle of around 70° from the original crack plane. At higher strain rate factor, failure occurs due to the shear localization originated from shear band formation ahead of the notch. The maraging steel used in the original experiments is X2 NiCoMo 18 9 5, and the counterpart material in the ANSI system is maraging steel 18Ni(300) (alternatively labeled as 18Ni1900 as in Belytschko et al. (2003), in which 1900 MPa represents material tensile strength in metric unit system, while 300ksi is measured in English units). The material properties are listed in Table 8. Notice the factor of notch tip radius in this problem: with a sharp crack, shear band damage mode can occur at even low impact loading rate. For the mesh used in this study, the notch tip is originally sharp ($r_0 = 0$), and theoretically it results in infinite v_0/r_0 ratio. However, the presence of cohesive elements eliminates stress singularity at the crack tip and introduce a finite separation at the crack tip. Moreover, when the notch tip is subjected to the influence of impinging stress wave, it does not retain a ($r_0 = 0$) shape.

Both the brittle failure and the shear band failure modes have been studied extensively (e.g., Zhou et al., 1998 for the latter case). In this study, we only attempt to simulate the brittle failure mode. Belytschko et al. (2003) modelled these experiments using the extended FEM (XFEM) with both loss of hyperbolicity criterion and tensile stress criterion. The overall crack propagation angle of around 58° was reported for the former, and 65° for the latter. The Virtual Internal Bond model combined with meshfree methods were employed by Klein et al. (2000), and produced an average crack growth angle of 63° and 79° depending on the texture of integration grid. Both studies also reported simulations using (Xu and Needleman, 1995) cohesive model, but with different mesh discretization and cohesive strength. In this study, we investigate the overall crack propagation angle, crack initiation time and

Table 8
Material properties of 18Ni(300) steel and cohesive model parameters used in simulating Kalthoff–Winkler Experiments Belytschko et al. (2003)

E (GPa)	v	ρ (kg/m³)	C_d (m/s)	G_{Ic} (kJ/m²)	T_n^{max} (GPa)	δ_n (μm)
190	0.3	8000	5654	22.2	1.733	25.63

propagation speed with a set of progressively refined element sizes. The impact loading rate is chosen as 16.54 m/s, following the work by Belytschko et al. (2003). Since the problem possesses symmetry, only half of the geometry is modelled, as shown in Fig. 29(b).

4.3.2. Bilinear cohesive model and initial stiffness considerations

The crack trajectory in this problem is not known *a priori*. In order to simulate crack propagation along arbitrary path, cohesive zone elements are inserted into a relatively large region through which the crack may potentially grow, as shown in Fig. 29(b). Initially, all bulk elements are bound together with cohesive force provided by the cohesive elements. Fracture occurs at high stress regions, where the local stress overcomes cohesive strength and the cohesive elements gradually lose resistance capability against separation, until complete decohesion takes place.

In the previous two examples where crack paths are predefined, there is essentially one line of cohesive elements added to the finite element mesh, and hence mesh refinement does not affect structure stiffness, as the total area of cohesive elements remains the same for various mesh discretizations. For the mixed-mode fracture problem under study, on the other hand, mesh refinement implies that larger total area of cohesive elements are inserted, along with larger capacity to dissipate energy, and addition of artificial compliance to the system. Therefore, the bilinear model discussed in Section 3.3 is adopted in this study in favor of its adjustable initial slope.

The material property and typical cohesive model parameters used in this study are given in Table 8. Due to lack of experimental information about the CZM parameters, we assume

$$G_{\mathrm{IIc}} = G_{\mathrm{Ic}}, \quad T_{\mathrm{t}}^{\max} = T_{\mathrm{n}}^{\max}, \quad \delta_{\mathrm{t}} = \delta_{\mathrm{n}},$$

where the fracture toughness of opening and sliding modes are related to cohesive strengths and critical openings as

$$G_{\mathrm{Ic}} = \tfrac{1}{2} T_{\mathrm{n}}^{\max} \delta_{\mathrm{n}}, \quad G_{\mathrm{IIc}} = \tfrac{1}{2} T_{\mathrm{t}}^{\max} \delta_{\mathrm{t}}$$

for the bilinear cohesive model. In this study, the cohesive strength adopted in the bilinear model is relatively low ($T_{\mathrm{n}}^{\max} = E/110$) as compared to the usual case when the model by Xu and Needleman (1995) is employed ($T_{\mathrm{n}}^{\max} = E/10$). However, a stiff initial slope is chosen ($\lambda \leqslant 0.01$) to limit the artificial compliance introduced. For example, when a 80×80 grid mesh is used, the additional compliance introduced can be estimated as (Zavattieri and Espinosa, 2001)

$$E_{\mathrm{add}} = \frac{T_{\mathrm{n}}^{\max}}{\lambda_{\mathrm{cr}} \delta_{\mathrm{n}}} \times h = \frac{E/110}{0.01(25.63 \times 10^{-6})} \times \frac{0.1/80}{3} = 14.8E,$$

where h is an equivalent cohesive element spacing estimated as grid spacing over number of cohesive elements within a unit grid. For these parameters, the additional elasticity introduced E_{add} within the cohesive elements region is much larger than the material Young's modulus E as long as the interface separation experienced by the cohesive elements does not exceed $\lambda_{\mathrm{c}} \delta_{\mathrm{n}}$. As the mesh is refined,

e.g., 100×80 and 120×120 grids, the initial slope is also adjusted to maintain the same value of E_{add}.

Two sets of calculations are carried out to investigate the capabilities of the bilinear cohesive model. The first set aims to study the effect of mesh orientation on the fracture propagating path. With sufficiently refined mesh, the crack is assumed to find the same path for different meshes. Three rectangular unit cells
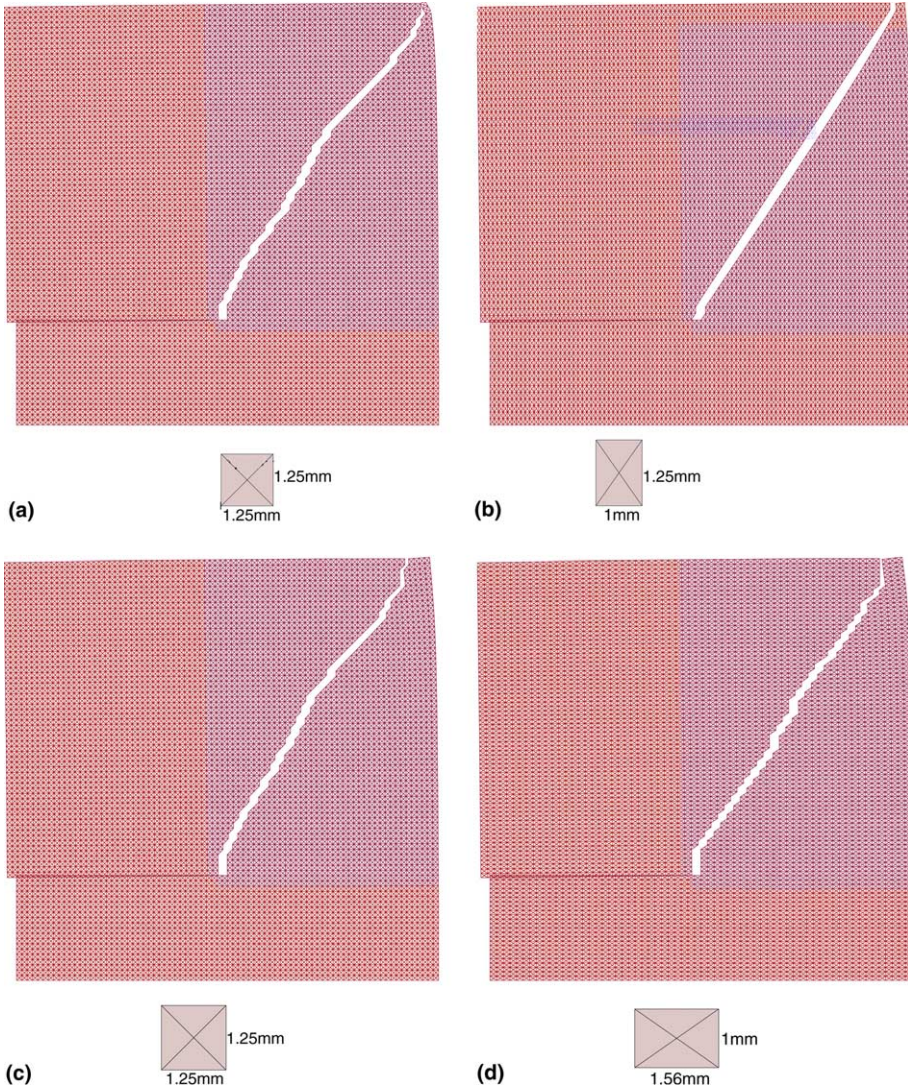

Fig. 30. Fracture path for different mesh designs considering $G_{IIc} = G_{Ic}$. The blue elements denote the region with cohesive elements, and all simulations use cohesive strength $T_n^{max} = E/110$ except for (c), which uses $T_n^{max} = E/30$; (a) 80×80 grid; (b) 100×64 grid; (c) 80×80 grid; (d) 64×100 grid.

with aspect ratios of *height/width* = {25/16,1,16/25} are considered. Therefore, the plate geometry is discretized into 64×100, 80×80 and 100×64 rectangles, each divided into 4 T6 elements. The second set of calculations investigate the effect of mesh size. Results obtained from 100×100 and 120×120 are compared to that from 80×80, for instance.

4.3.3. Results

The fracture paths for three aspect ratios of the ''unit mesh grid'' are shown in Fig. 30. These results indicate that, despite the different mesh orientation bias, the overall crack propagation paths of the three different meshes are similar. Notice that the crack path is not straight, but tends to propagate further towards the right surface when it moves closer to the boundary (see Fig. 30(a)). In order to avoid this ''boundary effect'', the crack angle is measured up to about first 2/3 crack length (the crack tip projection on *x*-axis is $x = 0.08$ m). The propagation angle is estimated to be around 72–74°, which agrees well with the experimental prediction (70°).

In all the cases shown in Fig. 30, the crack first propagates for a short distance at a right angle from the original crack path, and then zigzags through the inclined element edges and vertical edges in the meshes with grid aspect ratio of 1 and 25/16 (Fig. 30(a), (c) and (d)), while it propagates primarily along the inclined element edges for the remaining case of grid aspect ratio 16/25, resulting in an apparently smoother crack path (Fig. 30(b)). Additional calculation for the 80×80 grid mesh is carried out using a different cohesive strength $T_n^{max} = E/30$. The crack path is remarkably similar to the one with $T_n^{max} = E/110$ case, especially during the beginning stage of crack propagation. A close comparison of the final fracture pattern
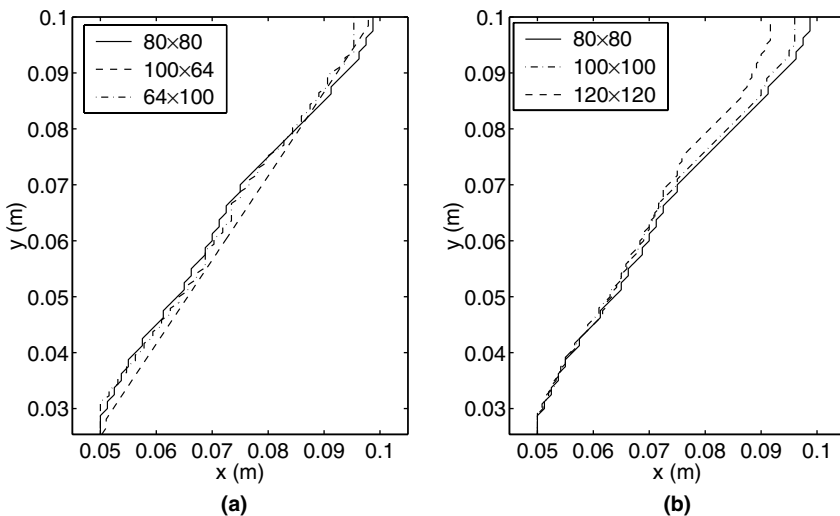

Fig. 31. Influence of mesh discretization on dynamic fracture behavior: (a) final crack paths for the first set of mesh discretization with total number of 25,600 T6 elements, and different mesh orientations and (b) final crack paths for square shape grids with element sizes $h = 1.25, 1, 0.8$ mm.

Table 9
Crack initiation time for different meshes

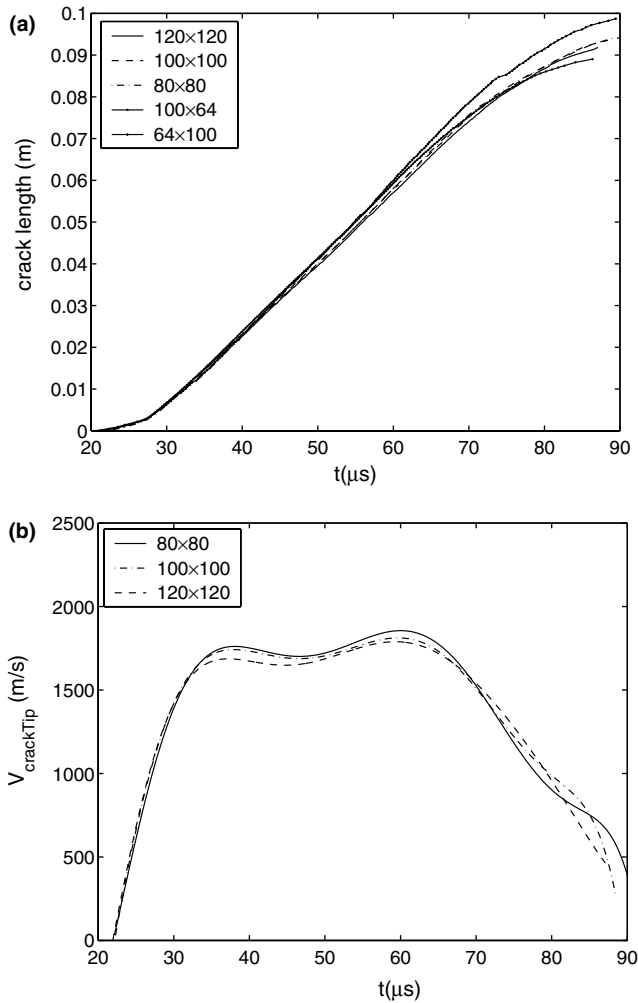| Mesh grid	Crack init. time (μs)	Mesh grid	Crack init. time (μs)	Mesh grid	Crack init. time (μs)
80 × 80	20.7	100 × 100	19.3	120 × 120	18.5
64 × 100	20.0	80 × 120	19.1	96 × 148	18.8
100 × 64	19.1	120 × 80	18.8	150 × 96	18.5

Fig. 32. Comparison of fracture path for different meshes: (a) crack length growth history and (b) smoothed crack velocity history.

for the three different mesh orientations is shown in Fig. 31(a). Clearly, the crack finds similar paths in meshes with different aspect ratio bias.

Two different sets of meshes of further refinement are tested, with 100×100, 120×80, 80×120 grids, and 120×120, 150×96, 96×148 grids, respectively. Each set of three meshes represent the three different aspect ratios discussed above. Although not all the results are reported here, the simulations demonstrate very similar global crack path for these settings, e.g., as shown in Fig. 31(b) for mesh with aspect ratio of 1. The computational crack initiation times are summarized in Table 9.

Crack length versus time is plotted in Fig. 32 (a) for 5 typical meshes used in the study. Clearly, the crack evolution with time maintains similar speed in all the cases
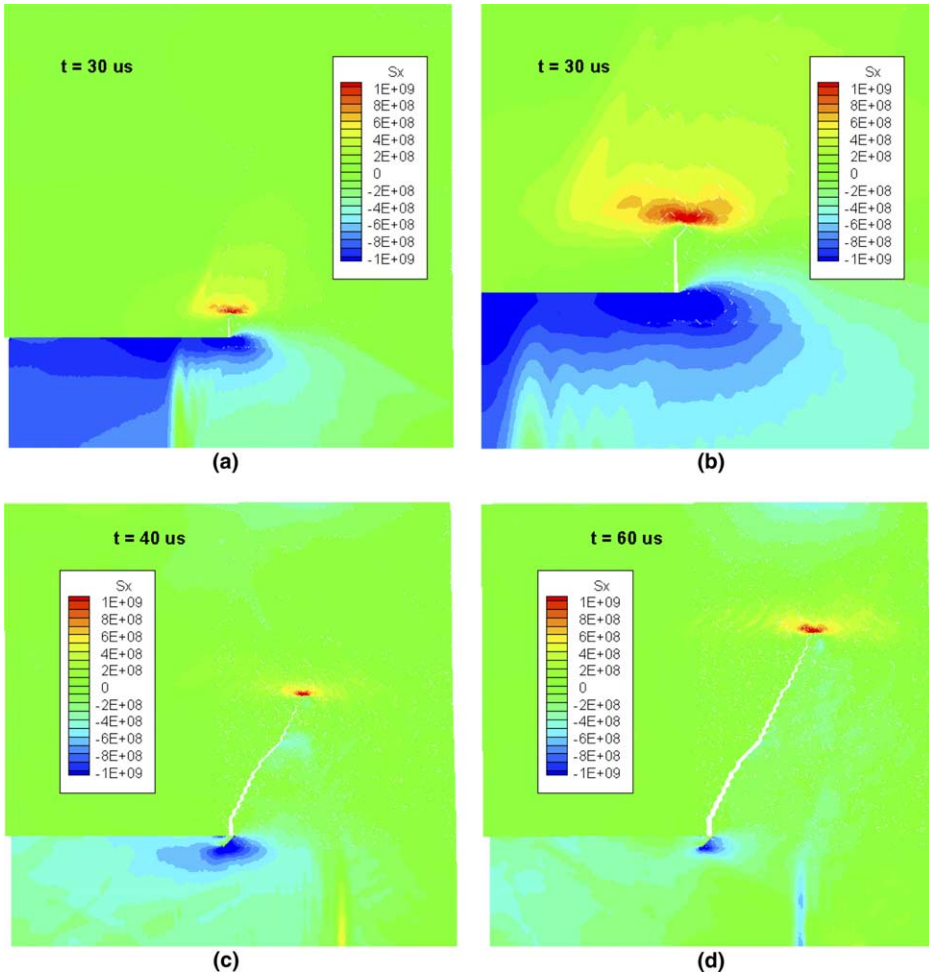

Fig. 33. Stress field σ_x and crack evolution in a 120×120 grid mesh: (a) crack pattern at $t = 30$ μs after crack propagation starts, (b) close-up of stress field at crack tip at $t = 30$ μs, (c) crack pattern at $t = 40$ μs and (d) crack pattern at $t = 60$ μs.

investigated. When computing the crack speed using discrete data at each time step, local oscillation of relatively small amplitude occurs due to mesh discretization effect involved in crack propagation. In order to focus on the global crack speed variation trend instead of local oscillation, the smoothened crack tip speed is calculated by taking derivative of a polynomial fitting curve of crack length. The crack tip velocity is thus plotted in Fig. 32(b). After crack initiation, the crack speed maintains a relatively steady speed around 1800 m/s, about 65% of the Rayleigh wave speed. This value is similar to that reported by Belytschko et al. (2003).

Although the overall crack path follows a slanted direction, the initial crack propagation always shows a short vertical segment in all the mesh cases studied. Other researchers (Klein et al., 2000; Belytschko et al., 2003) also reported similar results when using the cohesive model approach. This is not incidental, and the stress contour plots in Fig. 33 illustrate the critical role of wave propagation and reflection on the crack propagation direction. When the load is applied along the left edge of the lower plate section (below the initial crack plane), it creates compressive waves which propagate continuously rightwards along the lower plate section. Before the first tide of stress waves reach the initial crack tip, the stress distribution across the height direction of the lower section is fairly uniform, while the upper plate section remains stress-free. When the wave reaches the crack tip, the upper crack surface near the crack tip stays stationary, while the lower crack surface near the crack tip is under the influence of a rightward compressive wave. This creates a tearing effect at the crack tip. Afterwards, the waves continue to propagate rightwards in the lower plate section as compressive wave, and also propagate around the crack tip into the upper section (above the initial crack plane) of the plate. The stress waves along the upper crack surface are now tensile propagating towards left edge. Therefore the upper and lower surfaces of the crack are subjected to influence of stresses of opposite sign and direction along the Cartesian x coordinate, and a strong tearing effect is created at the crack tip. The principle tensile stress at the crack tip is thus in x direction, and the crack tip begins to open up and propagate in vertical direction when the local stress built up is high enough to overcome the cohesive strength. This initiation time occurs around 19 μs (Table 9). The crack maintains vertical path until the reflective wave from the right boundary reaches the crack tip region. The additive stress wave is now tensile, and when it interferes with the initial crack tip stress field, the principle tensile stress is no longer in pure x direction, and thus results in a slanted crack path. The crack turning time for different meshes are reported in Table 10. Clearly, all the cases indicate a similar time instant of around 28 μs, which is approximately the time needed for the first tide of the reflective waves to reach the crack tip:

Table 10
Crack turning time for different meshes (see Fig. 33(b))

Mesh grid	Crack deviation time (μs)	Mesh grid	Crack deviation time (μs)	Mesh grid	Crack deviation time (μs)
80×80	28.4	100×100	28.2	120×120	28.3
64×100	29.9	80×120	29.7	96×148	30.1
100×64	27.8	120×80	28.1	150×96	28.4

$$t_{\text{turn}} \approx \frac{1.5 \times W}{C_{\text{d}}} = \frac{1.5 \times 0.1}{5654} = 26.5 \ \mu s,$$

where W is the width of the specimen.

Another interesting issue is the different toughness associated with Mode I and Mode II fracture modes. In Section 4.3.2, we assumed that both the opening and sliding modes have the same fracture toughness. This assumption is not strictly true for real materials, which generally possess higher sliding toughness than opening toughness. Material property manuals usually only report the Mode I fracture toughness, as opening fracture is the dominant failure mode, and the experimental techniques for measuring the Mode I fracture toughness are far more mature than those for the Mode II toughness. To test how significant the aforementioned assumption influences the fracture behavior, we further carried out simulations using different sliding fracture toughness:

$$G_{\text{IIc}} = 3G_{\text{Ic}}, \quad T_{\text{t}}^{\text{max}} = T_{\text{n}}^{\text{max}},$$

$$G_{\text{IIc}} = 3G_{\text{Ic}}, \quad T_{\text{t}}^{\text{max}} = 3T_{\text{n}}^{\text{max}},$$

while the Mode I fracture parameters are maintained the same as before. Fig. 34 presents the crack trajectories in the two cases. Further comparison of these two specimens with $G_{\text{IIc}} = G_{\text{Ic}}$ specimen are summarized in Fig. 35. Evidently, the simulated fracture paths (cf. Fig. 34(a) and (b), and Fig. 35(a)) using different G_{IIc} values are close, especially during the beginning stage of crack growth. It is easily understood that the overall crack velocity (Fig. 35(b)) is slower for simulations using higher G_{IIc}
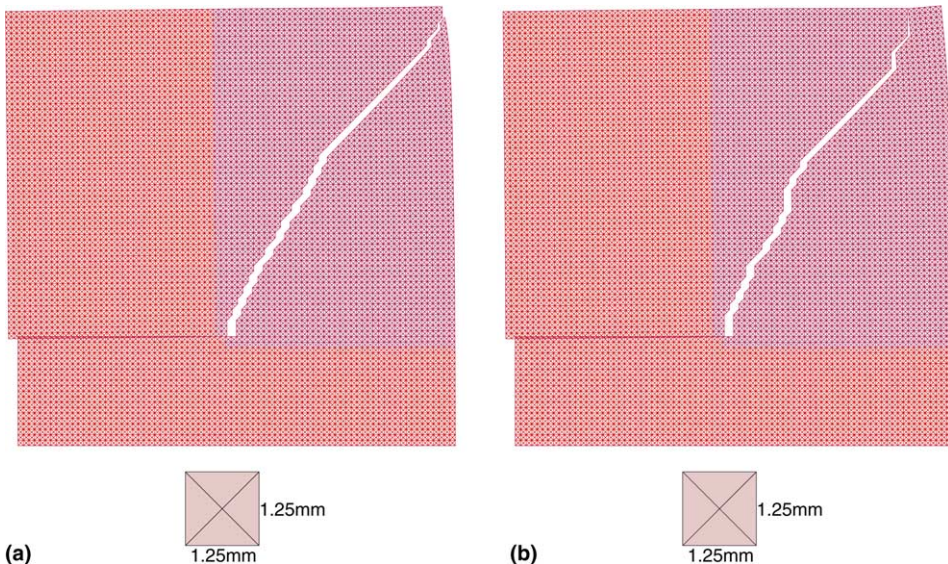

Fig. 34. Crack path for fracture toughness $G_{\text{IIc}} = 3G_{\text{Ic}}$. The blue elements denote the region with cohesive elements and simulations are performed using 80×80 grid meshes: (a) $T_{\text{t}}^{\text{max}} = T_{\text{n}}^{\text{max}}$ and (b) $T_{\text{t}}^{\text{max}} = 3T_{\text{n}}^{\text{max}}$.
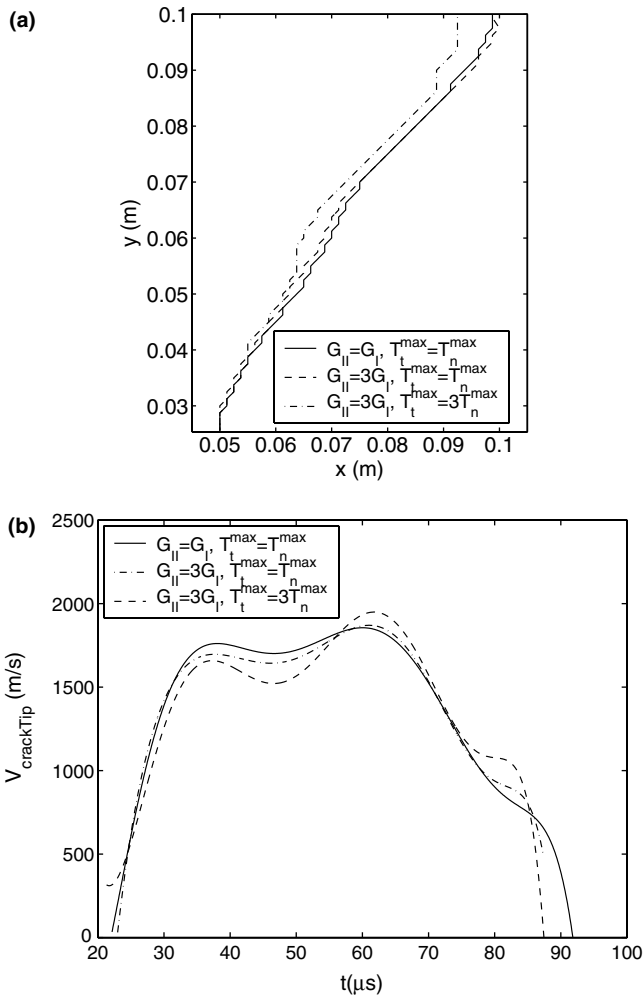
Fig. 35. Influence of different Mode II and Mode I fracture toughness ratios: $G_{IIc} = G_{Ic}$ and $G_{IIc} = 3G_{Ic}$: (a) final crack paths and (b) smoothed crack velocity history.

values, as increased toughness hinders crack propagation. However, the difference is minor and the overall trends of crack growths are similar. Within the limited scope of the present work, the underlying mechanism to explain the relatively minor influence of different sliding toughness is that when the crack advances, the local crack growth is controlled by the opening fracture mode, so that as long as the Mode I toughness used in the simulations are the same, the fracture behaviors are similar. On the other hand, the mode toughness ratio $G_{IIc}/G_{Ic} = 3$ used in the simulation is moderate. Other mode toughness ratios are tested, and the trend of crack paths (including that shown in Fig. 35) suggests that with higher sliding toughness and higher sliding strength, the crack growth angle, particularly the part towards the

"boundary", is closer to an overall angle of 70°, the experimental result. However, this issue certainly warrants further investigation.

4.3.4. Influence of material variation

Following the homogeneous material example, this section extends the study to simulation of the same experimental setting with graded material properties. For the sake of comparison with the previous results, the hypothetical material properties used in this section are conceived based on the homogeneous maraging steel described in Table 8. Although the variation of a wide range of material property parameters will contribute to changing fracture behavior, this study focuses on two of the most important material properties in dynamic fracture problem. One is the fracture toughness, as it is directly related to the material resistance capacity; and the other is material stiffness, as it is related to wave propagation velocity and local stress level. To isolate the influence of different parameters on the fracture behavior, first the simulation is carried out with graded fracture parameters (including fracture toughness and cohesive strength), and next with both graded Young's modulus and fracture parameters (including fracture toughness and cohesive strength).

4.3.4.1. Graded cohesive strength and fracture toughness. Consider a linear variation of fracture toughness G and cohesive strength T_n^{max} inside the cohesive region along the Cartesian x-direction, i.e., $G(x)$ and $T_n^{max}(x)$. The material properties are given in Table 11, where subscript 1, 2 and *tip* denote the left side, right side and the initial crack tip of the specimen. The material properties for the homogeneous specimen are also included. For the graded specimens, the bulk material remains homogeneous, and the fracture toughness gradation within the cohesive element region is linear. The Mode-I and Mode-II fracture toughness and cohesive strength are assumed to be the same, i.e., $G_{Ic} = G_{IIc}$, $T_n^{max} = T_t^{max}$. The specimen with $G(W) = 2G(0)$ is denoted as "LHS weaker" case, while the other one with opposite material gradation profile (i.e., $G(0) = 2G(W)$) is denoted as "RHS weaker" case.

Since the bulk material is homogeneous, the wave propagation speed is constant for all three cases, and the stress carried by the wave propagation builds up at the crack tip at the same rate. The critical stage of crack initiation depends on the local material toughness, and presumably takes place earlier for the specimen weaker at the initial

Table 11
Material property for pre-notched plate with graded fracture toughness, which is subjected to mixed-mode dynamic loading

Material	E (GPa)	C_d (m/s)	G_1 (kJ/m^2)	G_{tip} (kJ/m^2)	G_2 (kJ/m^2)	T_1^{max} (GPa)	T_{tip}^{max} (GPa)	T_2^{max} (GPa)	λ_{cr}	t_{init} (μs)
Homogeneous	190	5654	22.2	22.2	22.2	1.733	1.733	1.733	0.01	20.7
FGM-LHS weaker	190	5654	22.2	22.2	44.4	1.733	1.733	3.466	0.01	20.7
FGM-RHS weaker	190	5654	44.4	44.4	22.2	3.466	3.466	1.733	0.01	26.6

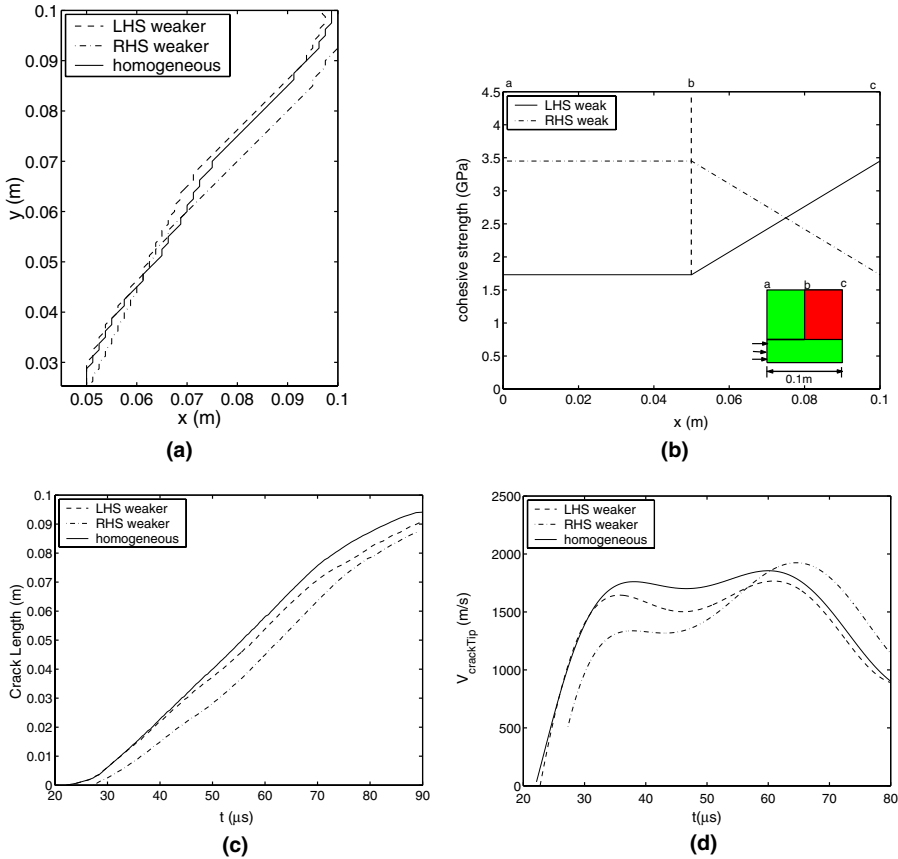The bulk material is homogeneous.

Fig. 36. Comparison of fracture path for different cohesive toughness and strength gradation profiles. Results obtained using 80 by 80 grid mesh: (a) final crack paths, (b) two cohesive strength gradation profiles. cohesive strength varies between $E/110$ to $E/55$ within the cohesive region; case 1: fracture toughness and cohesive strength are lower at LHS; case 2: fracture toughness and cohesive strength are lower at RHS, (c) crack length versus time and (d) crack tip speed versus time.

crack tip. The results are compared in Fig. 36 for the graded specimens with the homogeneous case of same mesh discretization and time step control.

As expected, the specimen with lower cohesive strength at crack tip ("LHS weaker" case in Fig. 36(b)) experiences crack initiation earlier. For this material profile, the cohesive strength is the same as in the homogeneous case, hence the crack initiation times for the two cases are almost identical ($t_{init} = 20.7$ µs for both cases, see Table 11). The crack initiation time for "RHS weaker" specimen is around $t_{init} = 26.6$ µs, close to the time when the reflected waves reach the crack tip, and therefore the crack starts to propagate at a slanted angle, instead of along the vertical direction as in the homogeneous case. One observes that as the fracture toughness is

graded, the crack tends to propagate more into the weaker region (Fig. 36(a)), while the homogeneous case is in between of the two graded cases.

The influence of fracture toughness on dynamic crack propagation can also be observed in the crack speed evolution profile (Fig. 36(c) and (d)). For the homogeneous case, the average fracture toughness is lower than the graded material cases, resulting in lower resistance against crack advance, and thus the overall crack speed is highest among the three. The "LHS weaker" specimen possesses similar material properties compared to the homogeneous case at the region where the crack starts to propagate, therefore the initial crack speed is also similar to that of the homogeneous one. As the crack propagates into tougher regions, the crack speed becomes slower than that of the homogeneous case. On the other hand, the "RHS weaker" specimen exhibits the reverse behavior: the crack speed is slower in the beginning, and then accelerates as the crack advances into the region of lower fracture resistance.

4.3.4.2. Graded modulus, cohesive strength and fracture toughness. The next set of simulations consider linearly graded Young's modulus E, fracture toughness G and cohesive strength T_n^{max} along the Cartesian x direction, i.e., $E(x)$, $G(x)$ and $T_n^{max}(x)$. The material properties are given in Table 12. The average material properties for the two graded specimens are the same as those of the homogeneous case, and the specimen which possesses E and G values at the right-hand-side twice as high as the left-hand-side is denoted as "LHS softer" case, while the other one with opposite material gradation profile is denoted as "RHS softer" case. Since the bulk material is graded, the wave propagation speed varies for the FGM case, while it is constant for the homogeneous case.

The crack paths and evolutions with time are plotted in Fig. 37 for the graded specimens as well as the homogeneous case. Apparently, the crack tends to grow into the weaker region (Fig. 37(a)). After the velocity loading is applied to the lower left surface, the stress waves propagate rightwards and the stress concentration builds up at the crack tip. Since the material fracture toughness at the initial crack tip ($x = 0.05$ m, $y = 0.0275$ m) are the same for all three cases, the crack initiation time is primarily determined by the rate of stress concentration at the crack tip. Because the material stiffness varies along the x direction, the stress waves propagate at varying speeds. For the "RHS softer" specimen, the average stiffness between the left surface (where the load is applied) and the crack tip is higher than the other two cases, and consequently the average wave speed is faster. Therefore, it takes shorter time for the

Table 12
Material property for pre-notched plate with graded modulus, fracture toughness and cohesive strength, which is subjected to mixed-mode dynamic loading

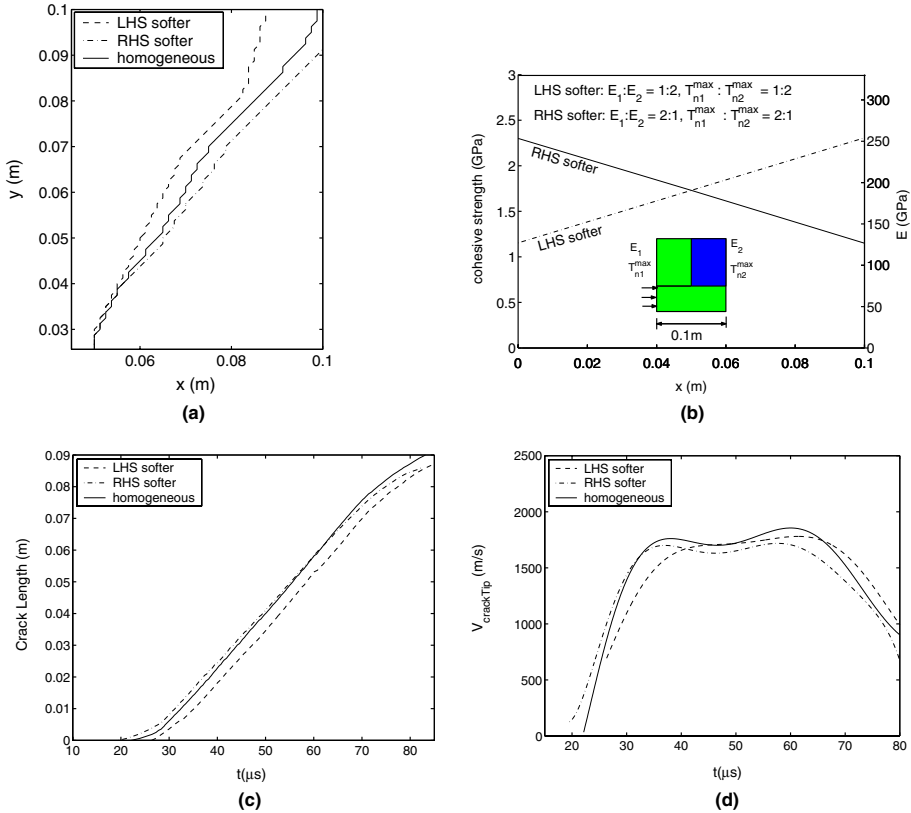| Material	E_1 (GPa)	E_{tip} (GPa)	E_2 (GPa)	G_1 (kJ/m^2)	G_{tip} (kJ/m^2)	G_2 (kJ/m^2)	T_1^{max} (GPa)	T_{tip}^{max} (GPa)	T_2^{max} (GPa)	t_{init} (μs)
Homogeneous	190	190	190	22.2	22.2	22.2	1.733	1.733	1.733	20.7
FGM-LHS softer	127	190	253	14.8	22.2	29.6	1.155	1.733	2.301	24.8
FGM-RHS softer	253	190	127	29.6	22.2	14.8	2.301	1.733	1.155	18.2

Fig. 37. Comparison of fracture paths for graded stiffness and graded fracture toughness along the Cartesian x direction. Results obtained using 80 by 80 grid mesh: (a) final crack paths, (b) material gradation profiles for E and cohesive strength. Case 1: material is softer and has lower fracture toughness at LHS; case 2: material is softer and has lower fracture toughness at RHS; average E and T_n^{max} are kept the same as the homogeneous case, (c) crack length versus time and (d) crack tip speed versus time.

crack tip tensile stress to reach the critical value for this case than the opposite material gradation case, and thus the crack initiates earlier. The crack initiation time for the "RHS softer" specimen ($T_{init} = 18.2$ μs) is 6.6 μs earlier than the "LHS softer" specimen ($T_{init} = 24.8$ μs), while the homogeneous case exhibits a crack initiation time in between ($T_{init} = 20.7$ μs), as shown in Table 12 and Fig. 37(c). After crack initiation, two factors control crack propagation speed: the local fracture toughness represented by the cohesive properties, and the crack extension driving force, which is related to the material stiffness, since the stress level resulting from forced displacement is lower in compliant material than in stiffer material. Therefore, when the crack in "RHS softer" specimen grows along a slanted direction into materials of gradually lower fracture toughness and lower stiffness, the lower fracture resistance tends to accelerate crack propagation, while the lower stress level accompanied by the compliant material tends to decelerate crack extension. The two effects partly

counteract each other. Similar effects are in action in the reversed material gradation profile case ("LHS softer" specimen). Therefore, it is not surprising that the difference in crack propagation velocities for the two cases and the homogeneous case is relatively small compared to the previous test with only cohesive strength graded (compare Fig. 36(d) and Fig. 37(d)).

5. Conclusions

In this study, the dynamic fracture behavior of homogeneous and functionally graded materials under dynamic loading is investigated. A research code is developed using *explicit* dynamic scheme with time step control due to varying wave speed in FGMs and presence of cohesive elements. Two basic types of elements are employed in the present investigation: *graded* elements in the bulk material, and *graded intrinsic cohesive* elements to model fracture. The graded elements are associated with non-homogeneous elastic constitutive relationships of the bulk material, and the graded cohesive elements are associated with traction–separation relationships to describe physical conditions at the crack tip (actual and fictitious) and the fracture evolution. Thus two competing length scales are present: one due to material gradation ($\ell_{\text{FGM}} = 1/\gamma$ if $E(x) = E_0 e^{\gamma x}$) and the other due to the fracture process ($\ell_k \sim (K_c/T_{\text{ave}})^2$), which have been discussed in the previous examples.

Intrinsic CZMs are investigated for FGMs, including the potential-based surface network approach based on effective quantities. The main drawbacks of this approach include the artificial compliance introduced with the embedded cohesive elements, the attenuation of crack tip stress singularity due to cohesive surface separation, and the crude approximation of mode mixity by using effective quantities. As an alternative, (Xu and Needleman, 1995) model was extended to treat FGMs, which eliminates the dependence upon effective quantities, and may provide certain advantages when mixed-mode effect is prominent and material toughness is significantly different for Mode-I and Mode-II fracture. Further, a bilinear model is adapted for the FGM case, which provides the advantage of adjustable initial stiffness. When cohesive elements are assigned in a large region, adjusting the traction–separation curve initial stiffness helps to limit the artificial compliance introduced into the computational framework and to maintain a comparable basis for meshes with different mesh discretization.

Examples are presented to verify the computational code and to investigate the dynamic fracture behavior of FGMs considering crack propagation in predefined and non-predefined paths. As illustrated in the study, the cohesive approach is promising for modeling generalized fracture without predefined fracture criteria. It proves to be an attractive alternative approach for investigating a broad range of fracture phenomena, especially for dynamic fracture propagation problems involving non-predefined crack paths. Comparison of results of numerical simulation with those from experiments indicates that the cohesive zone approach is capable of qualitatively capturing the fracture evolution characteristics in homogeneous and graded

materials, however, the quantitative match of results may require extensive calibration of cohesive zone model parameters.

Acknowledgments

References

Anderson, T.L., 1995. Fracture Mechanics: Fundamentals and Applications. CRC Press, Boca Raton, FL.

Anlas, G., Santare, M.H., Lambros, J., 2000. Numerical calculation of stress intensity factors in functionally graded materials. International Journal of Fracture 104, 131–143.

Aboudi, J., Pindera, M.-J., Arnold, S.M., 1999. Higher-order theory for functionally graded materials. Composites: Part B (Engineering) 30, 777–832.

Aboudi, J., Pindera, M.-J., Arnold, S.M., 2003. Higher-order theory for periodic multiphase materials with inelastic phases. International Journal of Plasticity 19, 805–847.

Barenblatt, G.I., 1959. The formation of equilibrium cracks during brittle fracture: General ideas and hypothesis, axially symmetric cracks. Applied Mathematics and Mechanics (PMM) 23, 622–636.

Barenblatt, G.I., 1962. Mathematical theory of equilibrium cracks in brittle fracture. In: Dryden, H.L., von Karman, T. (Eds.), Advances in Applied Mechanics, vol. 7, pp. 55–125.

Bathe, K.-J., 1996. Finite Element Procedures. Prentice-Hall, New Jersey.

Baylor, J., 1998. A Numerical Simulation of Impact-induced Damage of Composite Materials. Master Thesis, University of Illinois at Urbana-Champaign.

Bažant, Z.P., Cedolin, L., 1991. Stability of Structures: Elastic, Inelastic, Fracture and Damage Theories. Oxford University Press, New York.

Bažant, Z.P., Planas, J., 1998. Fracture and Size Effect: in Concrete and Other Quasibrittle Materials. CRC Press, New York.

Belytschko, T., Chen, H., Xu, J., Zi, G., 2003. Dynamic crack propagation based on loss of hyperbolicity and a new discontinuous enrichment. International Journal of Numerical Methods in Engineering 58, 1873–1905.

Belytschko, T., Chiapetta, R.L., Bartel, H.D., 1976. Efficient large scale non-linear transient analysis by finite elements. International Journal for Numerical Methods in Engineering 10, 579–596.

Belytschko, T., Liu, W.K., Moran, B., 2000. Nonlinear Finite Elements for Continua and Structures. Wiley, New York.

Brocks, W., Cornec, A. (Eds.), 2003. Cohesive models. Engineering Fracture Mechanics 70, 1741–1990 (special issue).

Camacho, G.T., Ortiz, M., 1996. Computational modeling of impact damage in brittle materials. International Journal of Solids and Structures 33, 2899–2938.

Chin, E.S.C., 1999. Army focused research team on functionally graded armor composites. Materials Science and Engineering A 259, 155–161.

Cornec, A., Scheider, I., Schwalbe, K-H., 2003. On the practical application of the cohesive model. Engineering Fracture Mechanics 70, 1963–1987.

Costanzo, F., Walton, J.R., 1997. A study of dynamic crack growth in elastic materials using a cohesive zone model. International Journal of Engineering Science 35, 1085–1114.

Detournay, E., Garagash, G.I., 2003. The near-tip region of a fluid-driven fracture propagating in a permeable elastic solid. Journal of Fluid Mechanics 494, 1–32.

Dolbow, J.E., Gosz, M., 2002. On the computation of mixed-mode stress intensity factors in functionally graded materials. International Journal of Solids and Structures 39, 2557–2574.

Dugdale, D.S., 1960. Yielding of steel sheets containing cracks. Journal of the Mechanics and Physics of Solids 8, 100–104.

Eischen, J.W., 1987a. Fracture of non-homogeneous materials. International Journal of Fracture 34, 3–22.

Eischen, J.W., 1987b. An improved method for computing the J_2 integral. Engineering Fracture Mechanics 26, 691–700.

Erdogan, F., 1995. Fracture mechanics of functionally graded materials. Composites Engineering 5, 753–770.

Freund, L.B., 1998. Dynamic Fracture Mechanics. Cambridge University Press, New York.

Falk, M.L., Needleman, A., Rice, J.R., 2001. A critical evaluation of dynamic fracture simulation using cohesive surfaces. Journal de Physique IV, Pr-5-43–Pr-5-50.

Geubelle, P.H., Baylor, J., 1998. Impact-induced delamination of laminated composites: a 2D simulation. Composites Part B Engineering 29, 589–602.

Gooch, W.A., Chen, B.H., Burkins, M.S., Palicka, R., Rubin, J., Ravichandran, R., 1999. Development and ballistic testing of functionally gradient ceramic/metal applique. Materials Science Forum 308–311, 614–621.

Hattiangadi, A., Siegmund, T., 2004. A thermomechanical cohesive zone model for bridged delamination cracks. Journal of the Mechanics and Physics of Solids 52, 533–566.

Jin, Z.-H., Paulino, G.H., Dodds Jr., R.H., 2002. Finite element investigation of quasi-static crack growth in functionally graded materials using a novel cohesive zone fracture model. ASME Journal of Applied Mechanics 69, 370–379.

Jin, Z.-H., Paulino, G.H., Dodds Jr., R.H., 2003. Cohesive fracture modeling of elastic-plastic crack growth in functionally graded materials. Engineering Fracture Mechanics 70, 1885–1912.

Kalthoff, J.F., Winkler, S., 1987. Failure mode transition at high rates of shear loading. In: Chiem, C.Y., Kunze, H.D., Meyer, L.W. (Eds.), International Conference on Impact Loading and Dynamic Behavior of Materials, pp. 185–195.

Kim, J.-H., Paulino, G.H., 2002a. Isoparametric graded finite elements for nonhomogeneous isotropic and orthotropic materials. ASME Journal of Applied Mechanics 69, 502–514.

Kim, J.-H., Paulino, G.H., 2002b. Mixed-mode fracture of orthotropic functionally graded materials using the finite element method and the modified crack closure method. Engineering Fracture Mechanics 14–16, 1557–1586.

Kim, J.-H., Paulino, G.H., 2002c. Finite element evaluation of mixed-mode stress intensity factors in functionally graded materials. International Journal for Numerical Methods in Engineering 53, 1903–1935.

Kim, J.-H., Paulino, G.H., 2003. T-Stress, mixed-mode stress intensity factors, and crack initiation angles in functionally graded materials: a unified approach using the interaction integral method. Computer Methods in Applied Mechanics and Engineering 192, 1463–1494.

Kim, J.-H., Paulino, G.H., 2004. Finite element simulation of crack propagation in functionally graded materials under mixed-mode loading. International Journal for Mechanics and Materials in Design 1, 63–94.

Knauss, W.G., Losi, G.U., 1993. Crack propagation in a nonlinearly viscoelastic solid with relevance to adhesive bond failure. ASME Journal of Applied Mechanics 60, 793–801.

Klein, P., Gao, H., 1998. Crack nucleation and growth as strain localization in a virtual-bond continuum. Engineering Fracture Mechanics 61, 21–48.

Klein, P.A, Foulk, J.W., Chen, E.P., Wimmer, S.A., Gao, H., 2000. Physics-based modeling of brittle fracture: Cohesive formulations and the application of meshfree methods. Sandia National Laboratory, Technical Report, SAND2001-8099.

Lee, Y., Prakash, V., 1999. Dynamic brittle fracture of high strength structural steels under conditions of plane strain. International Journal of Solids and Structures 36, 3293–3337.

Li, H., Chandra, N., 2003. Analysis of crack growth and crack-tip plasticity in ductile materials using cohesive zone models. International Journal of Plasticity 19, 849–882.

Miyamoto, Y., Kaysser, W.A., Rabin, B.H., Kawasaki, A., Ford, R.G., 1999. Functionally Graded Materials: Design, Processing and Applications. Kluwer Academic Publishers, Dordrecht.

Needleman, A., 1987. A continuum model for void nucleation by inclusion debonding. Journal of Applied Mechanics 54, 525–531.

Nemat-Nasser, S., Hori, M., 1993. Micromechanics: Overall Properties of Heterogeneous Materials. Elsevier Science Publishers, Netherland.

Ortiz, M., Pandolfi, A., 1999. Finite-deformation irreversible cohesive elements for three-dimensional crack-propagation analysis. International Journal for Numerical Methods in Engineering 44, 1267–1282.

Pandolfi, A., Ortiz, M., 2002. An efficient adaptive procedure for three-dimensional fragmentation simulations. Engineering with Computers 18, 148–159.

Papoulia, K.D., Sam, C.H., Vavasis, S.A., 2003. Time continuity in cohesive finite element modeling. International Journal for Numerical Methods in Engineering 58, 679–701.

Paulino, G.H., Jin, Z.-H., Dodds Jr., R.H., 2003. Failure of Functionally Graded Materials. In: Karihaloo, B. et al. (Eds.), Encyclopedia of Comprehensive Structural Integrity, vol. 2. Elsevier, Amsterdam, pp. 607–644.

Rice, J.R., 1968. Mathematical analysis in the mechanics of fracture. In: Liebowitz (Ed.), Fracture, an Advanced Treatise, vol. 2. Academic Press, New York, pp. 191–311.

Ruiz, G., Pandolfi, A., Ortiz, M., 2001. Three-dimensional cohesive modeling of dynamic mixed-mode fracture. International Journal for Numerical Methods in Engineering 52, 97–120.

Roe, K.L., Siegmund, T., 2003. An irreversible cohesive zone model for interface fatigue crack growth simulation. Engineering Fracture Mechanics 70, 209–232.

Rousseau, C.-E., Tippur, H.V., 2000. Compositionally graded materials with cracks normal to the elastic gradient. Acta Materialia 48, 4021–4033.

Rousseau, C.-E., Tippur, H.V., 2001a. Dynamic fracture of compositionally graded materials with cracks along the elastic gradient: experiments and analysis. Mechanics of Materials 33, 403–421.

Rousseau, C.-E., Tippur, H.V., 2001b. Influence of elastic gradient profiles on dynamically loaded functionally graded materials: cracks along the gradient. International Journal of Solids and Structures 38, 7839–7856.

Rousseau, C.-E., Tippur, H.V., 2002a. Evaluation of crack tip fields and stress intensity factors in functionally graded elastic materials: cracks parallel to elastic gradient. International Journal of Fracture 114, 87–111.

Rousseau, C.-E., Tippur, H.V., 2002b. Influence of elastic variations on crack initiation in functionally graded glass-filled epoxy. Engineering Fracture Mechanics 69, 1679–1693.

Soboyejo, W., 2003. Mechanical Properties of Engineered Materials. Marcel Dekker Inc., New York.

Suresh, S., Mortensen, A., 1998. Functionally Graded Materials, The Institute of Materials. IOM Communications Ltd., London.

Tvergaard, V., 1990. Effect of fiber debonding in a whisker-reinforced metal. Materials Science and Engineering A 125, 203–213.

Tvergaard, V., 2003. Cohesive zone representation of failure between elastic or rigid solids and ductile solids. Engineering Fracture Mechanics 70, 1859–1868.

Xu, X., Needleman, A., 1995. Numerical simulations of dynamic crack growth along an interface. International Journal of Fracture 74, 289–324.

Yin, H., Sun, L., Paulino, G.H., 2004. Micromechanics-based elastic model for functionally graded materials with particle interactions. Acta Materialia 52, 3535–3543.

Yoon, C., Allen, D.H., 1999. Damage dependent constitutive behavior and energy release rate for a cohesive zone in a thermoviscoelastic solid. International Journal of Fracture 96, 55–74.

Zavattieri, P., Espinosa, H., 2001. Grain level model analysis of crack initiation and propagation in brittle materials. Acta Materialia 49, 4291–4311.

Zhang, Z., 2003. Cohesive zone modeling of dynamic failure in homogeneous and functionally graded materials. Master Thesis, University of Illinois at Urbana-Champaign.

Zhou, M., Rosakis, A.J., Ravichandran, G., 1998. On the growth of shear bands and failure-mode transition in prenotched plates: a comparison of singly and doubly notched specimens. International Journal of Plasticity 14, 435–451.